Electronic Structure Contributions to O–O Bond Cleavage Reactions for Mn^{III}-alkylperoxo complexes

Samuel A. Brunclik, Adedamola A. Opalade, and Timothy A. Jackson*

The University of Kansas, Department of Chemistry and Center for Environmentally Beneficial Catalysis, 1567 Irving Hill Road, Lawrence, KS 66045, USA.

*To whom correspondence should be addressed:
Timothy A. Jackson
Phone: (785) 864-3968
taj@ku.edu

Abstract

Synthetic manganese catalysts that activate hydrogen peroxide perform a variety of hydrocarbon oxidation reactions. The most commonly proposed mechanism for these catalysts involves the generation of a manganese(III)-hydroperoxo intermediate that decays via heterolytic O–O bond cleavage to generate a Mn(V)-oxo species that initiates substrate oxidation. Due to the paucity of well-defined Mn^{III}-hydroperoxo complexes, Mn^{III}-alkylperoxo complexes are often employed to understand the factors that affect the O–O cleavage reaction. Herein, we examine the decay pathways of the Mn^{III}-alkylperoxo complexes $[Mn^{III}(OO^{t}Bu)(^{6Me}dpaq)]^{+}$ and $[Mn^{III}(OO^{t}Bu)(N4S)]^{+}$, which have distinct coordination environments (N_5^- and N_4S^-, respectively). Through the use of density functional theory (DFT) calculations and comparisons with published experimental data, we are able to rationalize the differences in the decay pathways of these complexes. For the $[Mn^{III}(OO^{t}Bu)(N4S)]^{+}$ system, O–O homolysis proceeds via a two-state mechanism that involves a crossing from the quintet reactant to a triplet state. A high energy singlet state discourages O–O heterolysis for this complex. In contrast, while quintet-triplet crossing is unfavorable for $[Mn^{III}(OO^{t}Bu)(^{6Me}dpaq)]^{+}$, a relatively low-energy single state accounts for the observation of both O–O homolysis and heterolysis products for this complex. The origins of these differences in decay pathways are linked to variations in the electronic structures of the Mn^{III}-alkylperoxo complexes.

Introduction.

Mononuclear manganese catalysts that activate hydrogen peroxide (H_2O_2) are effective in a variety of hydrocarbon activation reactions, including asymmetric olefin epoxidation and late-stage C–H bond functionalization.[1-9] Because of the low-cost and abundance of manganese, the increased use of such catalysts could ameliorate some of the deleterious environmental impacts of chemical processes.[10-11] The mechanism most commonly proposed for these catalysts involves the formation of a Mn^{III}-hydroperoxo complex that decays by O–O heterolysis to yield a Mn^{V}-oxo species (steps *a* - *c* in Scheme 1).[3, 12] The Mn^{V}-oxo complex is invoked as the active species that initiates hydrocarbon oxidation (step *d* in Scheme 1). Despite the impressive performance of many of these catalysts, these systems require acid additives (~15 – 0.35 equiv. relative to substrate) for efficient H_2O_2 utilization,[2-3] and key steps in the mechanism remain incompletely understood.[1] A better understanding of the factors affecting the O–O cleavage step in particular could lead to the design of more effective catalysts that require fewer additives.

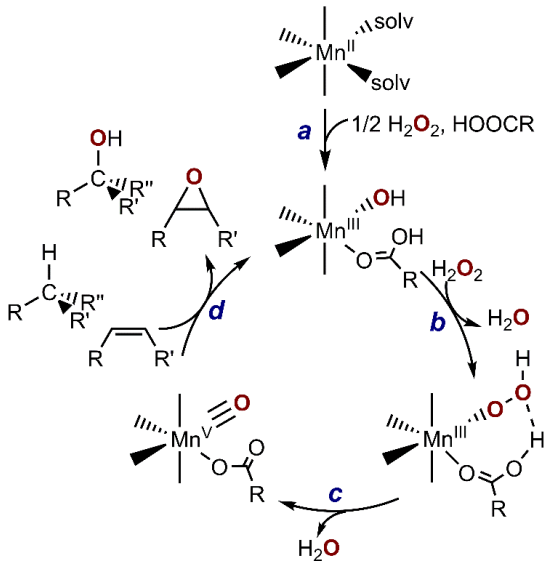

Scheme 1. Proposed mechanism for H_2O_2 activation and substrate (alkane or olefin) oxidation for Mn catalysts with N4 aminopyridyl ligands.

One of the key gaps in knowledge hindering our understanding of the O–O cleavage step of these catalysts is the scarcity of Mn^{III}-hydroperoxo complexes that have been trapped and spectroscopically characterized.[13-17] Nam and co-workers have reported Mn^{III}-hydroperoxo complexes supported by tetramethylcyclam (TMC) and a ring-contracted derivative.[14-15] These complexes have intense electronic absorption bands in the UV region (~400 – 300 nm) and resonance Raman data for $[Mn^{III}(OOH)(TMC)]^{2+}$ showed an $^{16}O/^{18}O$-sensitive band at 792 cm^{-1}.[15] Both of these Mn^{III}-hydroperoxo complexes can oxidize thioanisole,[14-15] but only one can oxidize hydrocarbons.[14] Studies of the reactivity of manganese(III)-hydroperoxo complexes have primarily focused on their ability to react directly with substrates.[14-15] Their decay pathways, especially by O–O cleavage, remain largely unexplored.

Metal-alkylperoxo complexes, which are typically more stable than their metal-hydroperoxo analogues, are often used to identify factors affecting O–O cleavage pathways.[18-23] This approach is justified by some Mn catalysts that have shown similar performance using either H_2O_2 or CmOOH as oxidant, which has been taken to suggest a common O–O activation mecahnism.[24-25] Studies of Mn^{III}-alkylperoxo complexes have already yielded important structure-reactivity correlations. Using a series of Mn^{III}-alkylperoxo complexes supported by pentadentate, thiolate-containing N4S ligands (Figure 1, left), Kovacs and co-workers observed that complexes with shorter O–O bonds showed slower thermal decay rates.[26] Moreover, the O–O bond lengths were inversely related to Mn–N bond lengths of equatorial 6-Me-pyridyl or quinolyl ligands (*i.e.*, shorter O–O bonds were associated with longer Mn–N bonds).[26] Examination of the decay of Mn^{III}-cumylperoxo complexes within this series showed exclusive formation of acetophenone as the organic product,[26-27] indicative of O–O homolysis (heterolysis would yield cumyl alcohol). Collectively, these observations demonstrate that the local geometry around the Mn^{III}-alkylperoxo

unit controls the decay rate for O–O homolysis. However, the particular decay pathway observed for these Mn^{III}-alkylperoxo complexes stands in contrast to that proposed for Mn^{III}-hydroperoxo intermediates formed in H_2O_2 activation reactions (Scheme 1). More recently, Kovacs and co-workers reported an $[Mn^{III}(OO^tBu)(N4O)]^+$ complex, where the thiolate-containing N4S ligand was replaced by an alkoxide-containing N4O analogue.[28] While the original $[Mn^{III}(OOR)(N4S)]^+$ complexes were thermally unstable, with half-lives at 25 °C of ~250 seconds, the $[Mn^{III}(OO^tBu)(N4O)]^+$ complex was remarkably stable, showing a half-life of >6000 seconds at 25 °C. This enhanced stability was attributed to the greater Lewis acidity of the Mn^{III} center in $[Mn^{III}(OO^tBu)(N4O)]^+$, which enhanced charge donation from the alkylperoxo π* MOs to the manganese(III) center and strengthened the O–O bond.[28]

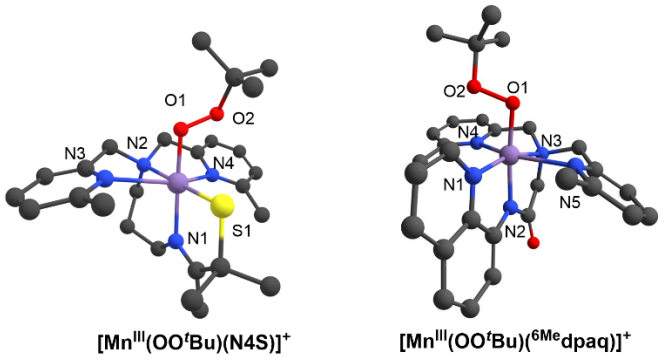

Figure 1. Structures of $[Mn^{III}(OO^tBu)(N4S)]^+$ (left) and $[Mn^{III}(OO^tBu)(^{6Me}dpaq)]^+$ (right) complexes. Hydrogen atoms have been omitted for clarity.

To broaden understanding of the role of the ligand environment in controlling the properties of Mn^{III}-alkylperoxo complexes, we generated several complexes using amide-containing N5 ligands.[29-30] The initial complexes in this series were only stable at lower temperatures (-15 °C), and a large excess of ^{t}BuOOH was required to form the Mn^{III}-alkylperoxo complexes in high yields.[29] To increase the stability of the Mn^{III}-alkylperoxo unit, we followed the correlation developed by Kovacs and co-workers,[26] and generated two new Mn^{III}-alkylperoxo complexes

using a ligand with 6-Me-pyridyl groups (^{6Me}dpaq; see Figure 1, right).[30] The 6-Me-pyridyl donors enforce long equatorial Mn–N bonds, which increase the stability of Mn^{III}-alkylperoxo complexes.[26-27] Both Mn^{III}-OO^{t}Bu and Mn^{III}-OOCm complexes of the ^{6Me}dpaq ligand were stable at 25 °C, which allowed us to determine the X-ray structure of [Mn^{III}(OOCm)(^{6Me}dpaq)](OTf).[30] Despite their high thermal stability, these complexes react directly with triphenylphosphine to give triphenylphosphine oxide and Mn^{II} products.[30] Thus, some geometric and/ or electronic feature renders these complexes more stable but also more reactive. An analysis of the thermal decay of [Mn^{III}(OOCm)(^{6Me}dpaq)]$^+$ in several solvents revealed acetophenone as a major product, marking O–O homolysis as the dominant decay pathway (70% in benzonitrile). However, cumyl alcohol was also observed as a decay product in all solvents (30% in benzonitrile), requiring that O–O heterolysis also occurs. This result differs from the exclusive decay of [Mn^{III}(OOCm)(N_4S)]$^+$ by O–O homolysis[26-27] and demonstrates that changes in the ligand sphere can be used to favor O–O heterolysis.

In this present work, we use density functional theory (DFT) computations to link differences in the decay pathways of Mn^{III}-alkylperoxo complexes to changes in the Mn^{III} coordination environments. We find that the presence of the π-acidic N4S ligand in [Mn^{III}(OO^{t}Bu)(N_4S)]$^+$ gives rise to a two-state reactivity mechanism, where a triplet spin state facilitates homolysis of the O–O bond. In addition, the thiolate ligand destabilizes decay pathways on the singlet surface, thus greatly disfavoring O–O heterolysis. In contrast, the N_5 coordination sphere of [Mn^{III}(OO^{t}Bu)(^{6Me}dpaq)]$^+$ leads to barriers for O–O homolysis and heterolysis within 3 kcal mol^{-1}, making both pathways competitive. The implications of these results with respect to Mn catalysts that activate H_2O_2 are discussed.

Computational Methods.

All electronic structure computations utilized the *ORCA* software program (versions 4.2.1 and 5.0.3).[31-32] Geometry optimizations and frequency calculations used the TPSSh functional (*vide infra*),[33] with D3 dispersion corrections,[34-35] and the def2-SVP basis set for carbon and hydrogen with the larger def2-TZVP basis set for the manganese, nitrogen, oxygen, and sulfur.[36-37] The integration grids were set to 6 (for *ORCA 4.2.1*) with RIJCOSX integral transformation approximations[38] and auxiliary basis sets called by the AutoAux command. Calculations were performed for complexes in a variety of spin states, as discussed below. All open-shell species were considered at the spin unrestricted level. Frequency calculations were used to verify all species were either minima (no imaginary frequencies) or transition states (one imaginary frequency). Frequency calculations also provided zero-point energies, thermal energies, and entropy terms (vibrational, rotational, and translational). Single point calculations were performed with the large def2-TZVPP basis set for all atoms, a finer integration grid (Grid7 and GridX7 in *ORCA*), and a conductor-like polarizable continuum solvent model for acetonitrile. The use of a solvent model in the geometry optimizations had a minimal (<1 kcal mol^{-1}) effect on the relative energies of several reactants, transition states, and products, but, in some cases, the use of the solvent model lead to multiple negative frequencies that could not be eliminated. On the basis of the very similar energies for models optimized with and without solvent, we concluded that solvent was not required during the geometry optimizations.

Comparison of DFT Geometries and Energies of Mn^{III}-alkylperoxo Complexes. We assessed the ability of various density functionals to reproduce the Mn-ligand bond lengths observed in the X-ray crystal structures of $[Mn^{III}(OOCm)(^{6Me}dpaq)]^+$ and $[Mn^{III}(OO^tBu)(N_4S)]^+$.[26, 30] In general, all functionals do a reasonable job of predicting metric parameters, as most Mn-ligand bond

lengths are within 0.02 – 0.05 Å of their experimental values. The TPSS-D3 functional performs best in reproducing the O–O distance of $[Mn^{III}(OOCm)(^{6Me}dpaq)]^+$ but the corresponding distance in $[Mn^{III}(OO^tBu)(N_4S)]^+$ is too long by ~0.03 Å (Table S1). The B3LYP and M06L functionals provide more accurate distances for $[Mn^{III}(OO^tBu)(N_4S)]^+$, but predict O–O distances 0.02 – 0.04 Å shorter than the experimental value for $[Mn^{III}(OOCm)(^{6Me}dpaq)]^+$. The elongated Mn–N(pyridine) distances are the parameter most difficult to calculate. In the experimental structure of $[Mn^{III}(OOCm)(^{6Me}dpaq)]^+$, there is an an asymmetry in the Mn–N(pyridine) distances, with one distance ~0.1 Å longer than the other.[26, 30] In contrast, each DFT structure of $[Mn^{III}(OOCm)(^{6Me}dpaq)]^+$ shows essentially identical Mn–N(pyridine) distances (within 0.01 Å) and thus fails to reproduce this aspect of the experimental structure (Table S1). The inclusion of D3 dispersion corrections tends to cause a contraction in the Mn–N(pyridine) distance (Table S1), which typically leads to better agreement with experiment. When considering both experimental structures, the TPSS-D3 and TPSSh-D3 functionals do the best job reproducing the alkylperoxo O–O distance and the longer Mn–N(pyridine) distances for $[Mn^{III}(OOCm)(^{6Me}dpaq)]^+$. While the B3LYP-D3 functional best reproduces the structural parameters for $[Mn^{III}(OOR)(N_4S)]^+$, the TPSS-D3 and TPSSh-D3 functionals still perform quite well. We placed more weight on the alkylperoxo O–O distance and the longer Mn–N(pyridine) distances because variations in these distances correlate with changes in decay rates for a series of $[Mn^{III}(OOR)(N_4S)]^+$ complexes.[26] Of these functionals, we settled on the TPSSh-D3 functional due to its excellent prediction of structural parameters and because this functional was previously employed to examine the electronic structure of $[Mn^{III}(OOR)(N_4S)]^+$ complexes.[26]

Importantly, the choice of density functional used for the optimization had very little effect on the relative single-point energies of $[Mn^{III}(OO^tBu)(^{6Me}dpaq)]^+$ and $[Mn^{III}(OO^tBu)(N4S)]^+$ in

different spin states (quintet, triplet, and singlet; see Table S2). For example, when using the TPSSh-D3 functional for single-point energy calculations, the $[Mn^{III}(OO^tBu)(^{6Me}dpaq)]^+$ complexes optimized using the TPSS-D3, TPSSh-D3, and B3LYP-D3 functionals have quintet-triplet gaps of 8.0, 8.3, and 8.4 kcal mol^{-1}, respectively. Quintet-singlet gaps for $[Mn^{III}(OO^tBu)(^{6Me}dpaq)]^+$ using the same approach are within 1.0 kcal mol^{-1} regardless of the functional used for the geometry optimization. Similar results are obtained for $[Mn^{III}(OO^tBu)(N4S)]^+$ (Table S2).

In contrast to the low sensitivity of the total energy to the functional used for geometry optimizations, we observed notable differences in the single point energy calculations using different functionals. These results are summarized in Tables S3 and S4. For these calculations, we optimized the geometries of quintet, triplet, and singlet spin Mn^{III}-OO^tBu complexes using the TPSSh-D3 functional, and then calculated single point energies for these geometries using a variety of functionals. From these calculations, we observe a larger quintet-triplet and quintet-singlet gaps for functionals with greater Hartree-Fock exchange. Increasing the basis set used from triple-zeta to quadruple-zeta resulted in little change in energy (<0.5 kcal mol^{-1}; see Table S3). Although there is a strong influence of the chosen density functional on the spin state gaps, there are general trends in energy that are present for every functional considered. First, the $[Mn^{III}(OO^tBu)(^{6Me}dpaq)]^+$ complex has lower-lying triplet *and* singlet states than $[Mn^{III}(OO^tBu)(N4S)]^+$ regardless of the functional employed (Table S3). Second, the triplet-singlet gap for $[Mn^{III}(OO^tBu)(^{6Me}dpaq)]^+$ is almost always larger than that of $[Mn^{III}(OO^tBu)(N4S)]^+$. Thus, while any given functional might not yield absolute energies of different spin states in exact agreement with experiment, we expect that any trends dependent on different spin states should be treated in a reliable fashion. Most importantly, our goal with these

computational studies is *not* to identify a functional that precisely reproduces the experimental activation parameters. Instead, we seek to identify differences in electronic structure that contribute to the distinct experimental reactivities of these complexes. In this sense, we can still gain meaningful insight into the decay mechanisms of these complexes by reproducing the experimental trends, even if we are unable to exactly reproduce the experimental activation parameters.

Results and Analysis.

Relaxed Surface Scans for O–O Bond Cleavage. As an initial means of assessing the decay pathways of the Mn^{III}-alkylperoxo complexes, we performed relaxed surface scans by systematically varying the O–O distance from 1.45 to 3.00 Å. While experimental studies of $[Mn^{III}(OO^tBu)(^{6Me}dpaq)]^+$ and $[Mn^{III}(OO^tBu)(N_4S)]^+$ revealed high-spin ($S = 2$) Mn^{III} centers,[26, 30] the possible outcomes of O–O cleavage present a range of spin states (Scheme 2). Homolysis of the O–O bond generates a Mn^{IV}-oxo unit ($S = 3/2$) and a ^{t}BuO• radical ($S = ½$), which can spin couple to give either quintet or triplet spin systems. In contrast, heterolysis of the O–O bond would generate a Mn^{V}-oxo unit and a ^{t}BuO$^-$ anion. Both products are likely to be $S = 0$, giving a singlet spin system. We therefore considered quintet, triplet, and singlet spin states for our surface scans. This approach focuses on the critical O–O cleavage step and not on the ensuing pathways by which the final reaction products are formed.

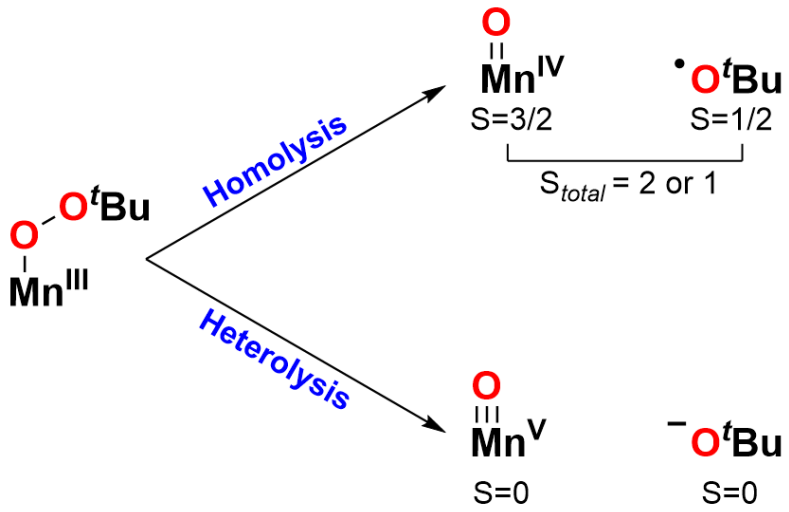

Scheme 2. Comparison of O–O homolysis and heterolysis pathways in the decay of a Mn^{III}–OO^tBu complex.

Elongation of the O–O bond on the quintet surface of each complex leads to a sharp rise in energy that plateaus at longer O–O distances (Figure 2). While $[Mn^{III}(OO^tBu)(N_4S)]^+$ shows a clear maximum near 2.1 Å, the maximum for $[Mn^{III}(OO^tBu)(^{6Me}dpaq)]^+$ is less pronounced and occurs later at 2.3 Å (Figure 2). The energy of this quintet surface also plateaus at longer O–O distances. On these quintet surfaces, the barrier for O–O cleavage for $[Mn^{III}(OO^tBu)(^{6Me}dpaq)]^+$ is slightly lower than that of $[Mn^{III}(OO^tBu)(N_4S)]^+$ (23.7 and 25.9 kcal mol^{-1}, respectively). In both cases, the products of O–O cleavage lie uphill energetically by ~20 - 23 kcal mol^{-1}. An analysis of the electronic structure of these S = 2 O–O cleavage products reveals Mn and O spin densities consistent with an S = 3/2 Mn^{IV}-oxo center ferromagnetically coupled to a $^tBuO\bullet$ radical (Scheme 2).

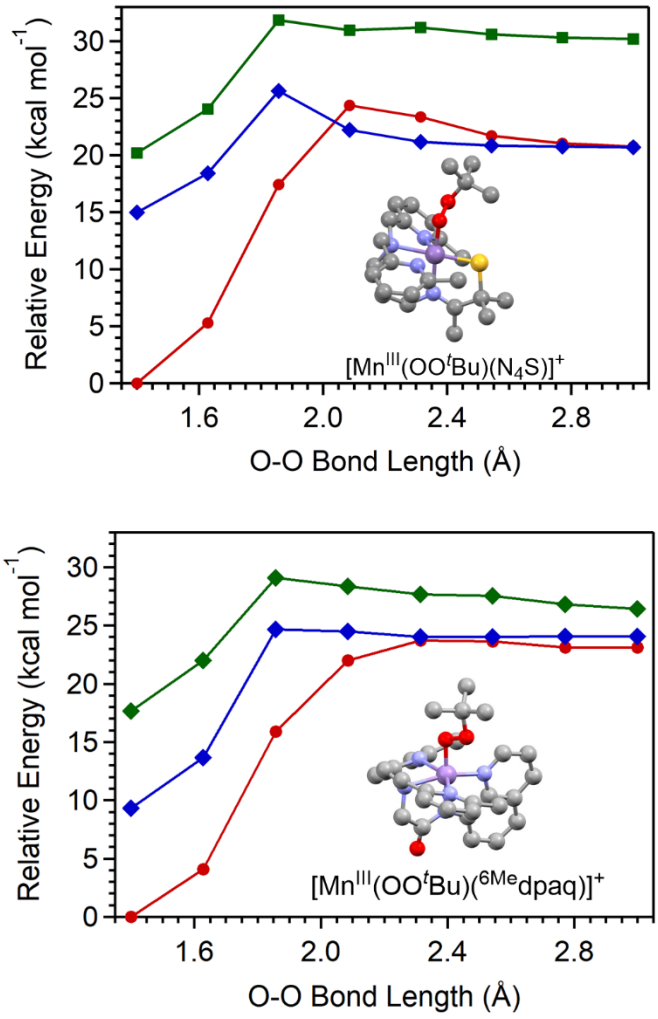

Figure 2. Relaxed surface scans of the quintet (red), triplet (blue), and singlet (green) spin states of $[Mn^{III}(OO^tBu)(N_4S)]^+$ (top) and $[Mn^{III}(OO^tBu)(^{6Me}dpaq)]^+$ (bottom) from DFT computations. In each step of the surface scan, the O–O bond of the Mn^{III}-alkylperoxo unit was fixed at a particular distance and all other atomic positions were fully optimized.

To further probe O–O homolysis pathways, we examined O–O elongation on the triplet (S = 1) surface. At short O–O distances, the triplet spin state consists of an intermediate spin Mn^{III} center, which is an excited state for both the $[Mn^{III}(OO^tBu)(^{6Me}dpaq)]^+$ and $[Mn^{III}(OO^tBu)(N_4S)]^+$ complexes. At the longest O–O separation of 3.0 Å, the triplet state consists of an S = 3/2 Mn^{IV}-oxo unit antiferromagnetically coupled to an S = ½ ^{t}BuO• radical (Scheme 2). For $[Mn^{III}(OO^tBu)(^{6Me}dpaq)]^+$ this state begins 9.3 kcal mol^{-1} above the quintet state, and the energy

of the triplet surface rises significantly with increasing O–O distance (Figure 2, bottom). The triplet surface becomes roughly isoenergetic with the quintet surface (24.0 kcal mol^{-1}) at O–O bond lengths greater than ~2.3 Å. For $[Mn^{III}(OO^tBu)(N_4S)]^+$, the triplet state begins at a higher relative energy (15 kcal mol^{-1}; see Figure 2, top). However, the energy of the triplet state of $[Mn^{III}(OO^tBu)(N_4S)]^+$ is less sensitive to elongation of the O–O bond length, and the triplet and quintet surfaces cross at an O–O distance of ~2.0 Å and an energy of 23 kcal mol^{-1}. Thus, O–O homolysis for $[Mn^{III}(OO^tBu)(N_4S)]^+$ could occur by a two-state mechanism, where the system thermally crosses from the quintet surface to the triplet surface during O–O elongation.

Finally, we considered the singlet states, which are involved in O–O heterolysis. For both complexes the singlet states begin and remain at highest energy along the entire reaction coordinate (Figure 2). The energy of these states begin ~20 kcal mol^{-1} above the quintet ground state and maximize (near 30 kcal mol^{-1}) at an O–O distance of 1.8 Å. The singlet state of $[Mn^{III}(OO^tBu)(N_4S)]^+$ remains high in energy (~30 kcal mol^{-1}) even at long O–O distances. In contrast, the singlet state of $[Mn^{III}(OO^tBu)(^{6Me}dpaq)]^+$ drops in energy at longer O–O distances (Figure 2, bottom). At the longest the O–O distance of 3.0 Å, the energy of the singlet state of $[Mn^{III}(OO^tBu)(^{6Me}dpaq)]^+$ (26 kcal mol^{-1}) is only ~2 - 3 kcal mol^{-1} above the triplet and quintet states.

Mn^{III}-alkylperoxo O–O Homolysis. Guided by the results of our surface scans, we developed reactants, transition states, and product complexes for O–O homolysis considering quintet and triplet spin states. Variable-temperature kinetic investigations for $[Mn^{III}(OO^tBu)(^{6Me}dpaq)]^+$ and $[Mn^{III}(OO^tBu)(N_4S)]^+$ have provided activation parameters ($\Delta H^‡$, $\Delta S^‡$, and $\Delta G^‡$), which allow us to evaluate our computations. In most of our discussion, we will compare $\Delta H^‡$, which we define

for the computations as the sum of the electronic, zero-point, and thermal energies. We will note $T\Delta S^{\ddagger}$ and $\Delta G^{\ddagger}$ values in certain cases.

A) Reactants, Transitions States, and Products for [Mn^{III}(OO^{t}Bu)(N4S)]$^{+}$. The O–O homolysis reaction for $[Mn^{III}(OO^{t}Bu)(N_4S)]^{+}$ begins on the quintet surface, as the triplet Mn^{III}-alkylperoxo species is higher in energy by 15.1 kcal mol^{-1} (Figure 3). The quintet $[Mn^{III}(OO^{t}Bu)(N_4S)]^{+}$ complex has a Mn $(d_{yz})^1(d_{xy})^1(d_{xz})^1(d_{x^2-y^2})^1(d_{z^2})^0$ configuration (we use a coordinate system with the z axis along the Mn–OO^{t}Bu bond and the x axis along the Mn–S bond). Among the t_{2g}-derived MOs, the Mn d_{xz} MO is at highest energy, as this MO is destabilized by strong π-antibonding interactions with an O–O π^* MO of the alkylperoxo ligand (Figure 3, left). The Mn d_{xy} MO, which is involved in a π-interaction with the thiolate ligand, is below the Mn d_{xz} MO. The Mn d_{yz} MO shows weak interactions with the O–O σ^* MO of the alkylperoxo ligand and is the lowest-energy Mn 3d orbital. The e_g-derived Mn $d_{x^2-y^2}$ and d_{z^2} MOs are involved in σ-interactions and lie at higher energies (Figure 3, left). In the triplet species, the lowest-energy d_{yz} MO is doubly-occupied, and the $d_{x^2-y^2}$ MO is unoccupied (Figure 3). As a consequence, the triplet reactant shows shorter Mn-ligand bonds with the equatorial donor atoms (Table 1). In particular, the Mn–N bonds involving the 6-Me-pyridyl groups contract by ~0.2 - 0.3 Å.

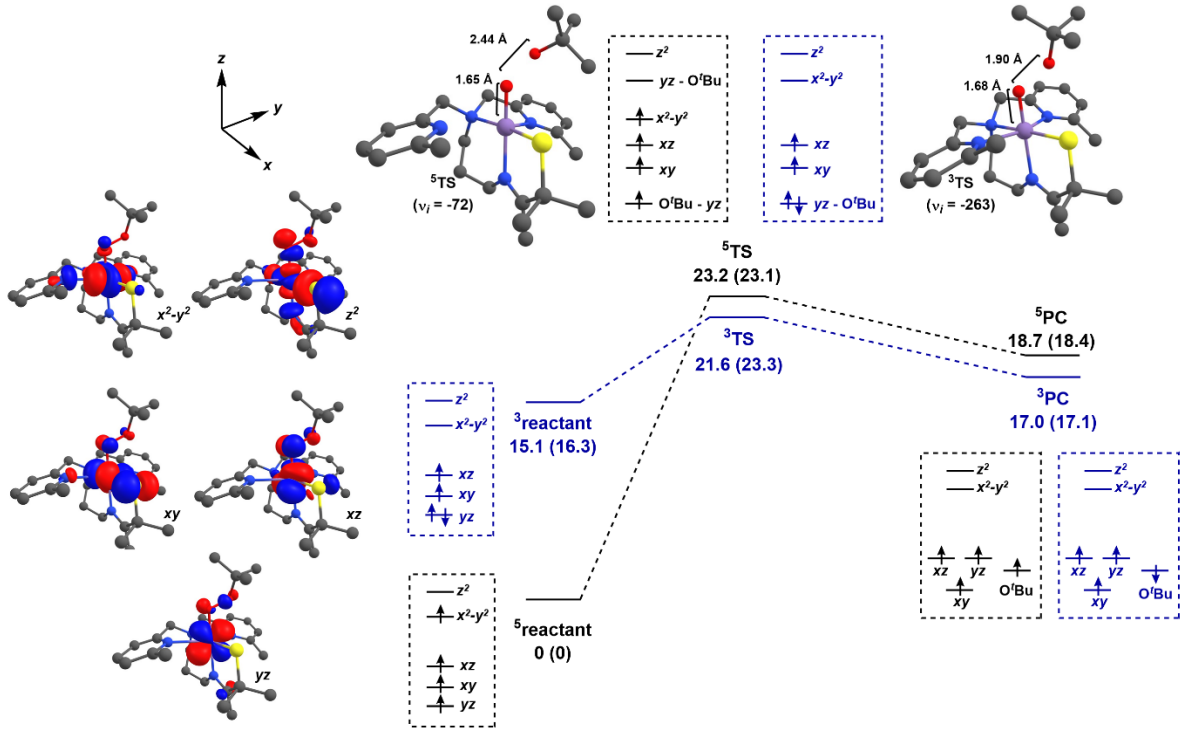

Figure 3. DFT-computed reaction coordinate for homolytic cleavage of the O–O bond of $[Mn^{III}(OO^tBu)(N4S)]^+$, with structures, electronic configurations, and MO plots of key species. Enthalpies and free energies (in parentheses) are in kcal mol^{-1}.

Because the relaxed surface scans for the quintet and triplet states cross before reaching a saddle point on the quintet surface (Figure 2, top), we performed a minimum energy crossing point (MECP) calculation to determine the structure at which these states are isoenergetic. The MECP structure is very early in the reaction coordinate, with an O–O bond of 1.46 Å and a Mn–O bond of 1.82 Å (Table S5). This MECP therefore precedes the transitions states on both surfaces. The MECP energy is 16.1 kcal mol^{-1} (ΔG = 16.8 kcal mol^{-1}), which is slightly higher than the triplet reactant energy (15.1 kcal mol^{-1}). The electronic structure of the quintet and triplet states at the MECP closely resembles those of the reactants (Table S5). Taken together, the results of the MECP calculations lend credence to a state crossing before reaching any O–O cleavage transition state.

Table 1. Selected Structural Parameters, DFT-computed Energies, and Mulliken Spin Densities for Reactants, Transition States (TS), and Product Complexes (PC) involved in the Homolytic Cleavage of the O–O Bond of $[Mn^{III}(OO^tBu)(N4S)]^+$.

	^{5}reactant	^{3}reactant	^{5}TS	^{3}TS	^{5}PC	^{3}PC
structural parameters[a]						
Mn–O1	1.84	1.82	1.65	1.68	1.65	1.65
O1–O2	1.45	1.46	2.44	1.90	3.39	2.64
Mn–S1	2.25	2.22	2.26	2.22	2.21	2.22
Mn–N1	2.09	2.12	2.12	2.19	2.21	2.20
Mn–N2	2.22	2.16	2.22	2.16	2.15	2.15
Mn–N3	2.50	2.22	2.69	2.20	2.15	2.17
Mn–N4	2.43	2.19	2.23	2.15	2.18	2.18
Mn–O1–O2	110.0	114.2	118.1	115.5	132.1	129.7
N1–Mn–O1	174.8	173.3	170.7	174.4	175.1	174.8
energies[b]						
E	0	13.9	24.9	21.8	19.1	19.0
ΔH	0	15.1	23.2	21.6	18.7	17.0
$T\Delta S$	0	-1.3	0.1	-1.8	0.3	-0.1
ΔG	0	16.3	23.1	23.3	18.4	17.1
spin densities						
Mn	3.97	1.90	3.55	2.22	2.44	2.43
O1	0.01	0.12	-0.51	0.36	0.56	0.53
O2	0.02	0.01	0.79	-0.55	0.86	-0.84
S1	-0.01	0.09	0.03	0.09	0.07	0.07

[a] Bond lengths in Å; bond angles in degrees. Atom numbering scheme is shown in Figure 1. [b] All energies in kcal mol^{-1}. The electronic energy E is taken from a single-point DFT calculation. The enthalpy (ΔH) is the sum of the electronic, zero-point, and thermal energies. The entropy term ($T\Delta S$) includes vibrational, rotational, and translational entropies is at 298 K. The free energy (ΔG) includes both the enthalpic and entropic terms.

The quintet and triplet transition states of $[Mn^{III}(OO^tBu)(N_4S)]^+$ are essentially isoenergetic, each lying ~22 kcal mol^{-1} above the quintet reactant.[39] The triplet transition state has a slightly lower enthalpy of activation than the quintet transition state, consistent with the state crossing observed in the surface scans. The transition state energies compare very well to the experimental $\Delta G^{\ddagger}$ of 20.4 kcal mol^{-1}, but they overestimate the experimental $\Delta H^{\ddagger}$ (15.9 kcal mol^{-1}; see Table 2).[26] The structures for these transition states are shown in Figure 3 (top), and metric parameters are summarized in Table 1. Both transition states lie late in the reaction coordinate, with short

Mn–O1 distances of less than 1.70 Å and O1–O2 separations of 1.90 Å or greater. The Mn–O1 distances are in the range observed for Mn^{IV}-oxo complexes from X-ray crystallographic and extended X-ray absorption fine structure (EXAFS) studies (1.63 – 1.72 Å).[40-46] Thus, in each transition state, the alkylperoxo O–O bond has been cleaved, yielding a Mn=O double bond and a ^{t}BuO moiety. A more detailed comparison of the quintet and triplet transition states reveals that the quintet is closer in geometry to the products. This transition state has a shorter Mn–O bond of 1.65 Å, and the O–O separation is quite long at 2.44 Å (Figure 3, top-left). The Mn–O bond in the triplet transition state is slightly longer (1.68 Å), and the O–O distance is notably shorter at 1.90 Å (Figure 3, top-right). The prediction that the triplet transition state lies earlier along the reaction coordinate is consistent with its position in the relaxed surface scan (Figure 2, top).

Table 2. Comparison of Calculated and Experimental Activation Parameters for the Decay of Mn^{III}-alkylperoxo Complexes by O–O Cleavage.

complex		spin state	$\Delta E^{\ddagger}$	$\Delta H^{\ddagger}$	$T\Delta S^{\ddagger}$	$\Delta G^{\ddagger}$
$[Mn^{III}(OO^{t}Bu)(^{6Me}dpaq)]^{+}$	experimental			21.4	-2.8	24.2
		quintet	25.1	23.4	0.4	23.0
		triplet	27.8	26.7	-1.7	28.4
$[Mn^{III}(OO^{t}Bu)(N_4S)]^{+}$	experimental			15.9	-4.5	20.4
		quintet	24.9	23.2	0.1	23.1
		triplet	21.8	21.6	-1.8	23.3

In spite of their relatively similar energies and comparable geometries, the quintet and triplet transition states show important differences in electronic structure. These differences are displayed, in complementary ways, through 1) the nature and occupancy of the frontier MOs (Figure 4), and 2) the calculated spin densities (Table 1). In both transition states, the frontier MOs now include a sixth orbital, originally derived from the alkylperoxo O–O σ* orbital. In the Mn^{III}-alkylperoxo reactants, this orbital is at high energy, but the pronounced O–O elongation in the transition state stabilizes this orbital considerably. Because the alkylperoxo O–O σ* MO has the

proper symmetry to mix with the Mn d_{yz} MO, the transition state frontier MOs contain MOs of mixed d_{yz} – O^{t}Bu character (Figure 4). In the quintet state, there is a lower-energy O^{t}Bu – d_{yz} MO with weakly interacting d_{yz} and O^{t}Bu units, with little density on the O1 atom (Figure 4). This MO will evolve to become the ^{t}BuO radical MO in the product. At higher energy is an unoccupied d_{yz} – O^{t}Bu MO with character predominantly on the Mn and O1 atoms (Figure 4). This MO will become a Mn=O π* MO in the product. For the triplet state, there are occupied α *and* β-spin d_{yz} – O$^{t\text{Bu}}$ MOs (shown as a doubly-occupied MO in Figure 4). These MOs resemble the doubly-occupied Mn d_{yz} MO in the triplet Mn$^{\text{III}}$-alkylperoxo reactant, but with increased character on the alkylperoxo unit. For the triplet species, the doubly-occupied d_{yz} - O^{t}Bu evolves to give the Mn d_{yz} MO (spin up) and ^{t}BuO radical MO (spin down) in the product.

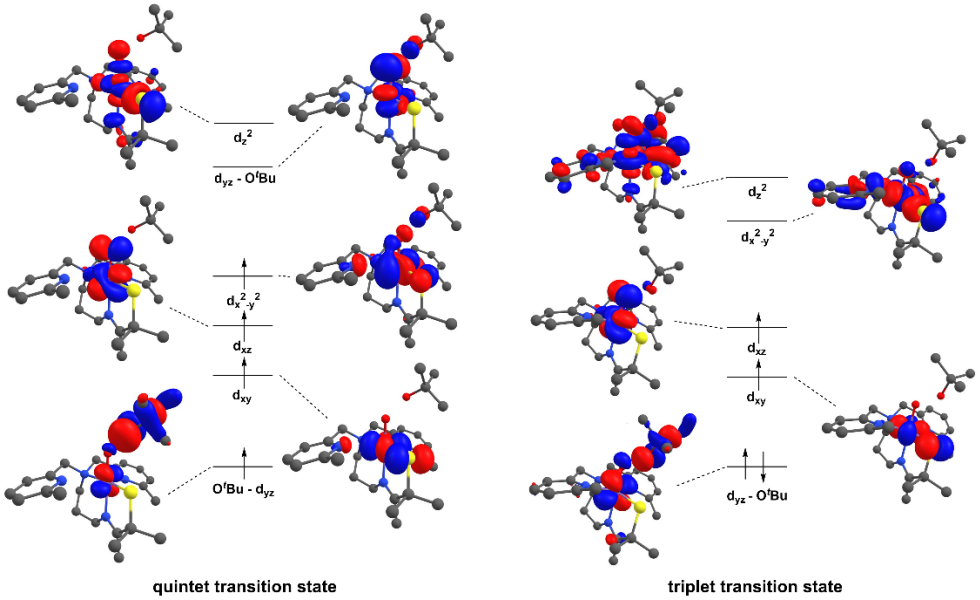

Figure 4. Surface contour plots (quasi-restricted MOs) and qualitative frontier MO splitting diagrams for the quintet (left) and triplet (right) transition states of [Mn$^{\text{III}}$(OO^{t}Bu)(N4S)]$^+$.

The difference in frontier MO occupancies for the quintet and triplet transition states of [Mn$^{\text{III}}$(OO^{t}Bu)(N4S)]$^+$ give rise to distinct spin densities. In the quintet spin state, the Mn-oxo unit shows oppositely signed spin densities (Mn and O1; see Table 1), with a large positive spin density

on Mn (3.55) and a small negative spin density on O1 (-0. 51). In contrast, the triplet spin state shows positive spin densities on both Mn and O1 (2.22 and 0.36, respectively). A brief discussion of the spin densities of isolated Mn^{IV}-oxo complexes will aid in classifying the differences between the quintet and triplet transition states. In the electronic ground state, six-coordinate Mn^{IV}-oxo complexes typically show a $(d_{xy})^1(d_{xz},d_{yz})^2(d_{x^2-y^2})^0(d_{z^2})^0$ configuration (Figure 5, left). The Mn 3d orbital splitting pattern reflects the strong covalency of the Mn-oxo unit. The d_{xz} and d_{yz} MOs are Mn-oxo π-antibonding, and thus lie above the d_{xy} MO, which is weakly π-antibonding with respect to the donors in the equatorial plane. Likewise, the d_{z^2} MO has strong σ-antibonding interactions with the oxo unit and therefore lies above the $d_{x^2-y^2}$ MO that is involved in σ-antibonding interactions with the equatorial ligands. This configuration gives rise to a $^4B_1$ ground state (using symmetry labels from the C_{4v} point group). Both DFT and CASSCF/NEVPT2 computations have shown that this $^4B_1$ state is characterized by positive spin density on both the Mn and O atoms of the Mn^{IV}-oxo unit (Figure 5, left).[47-48] This situation is caused by the high Mn-oxo covalency in the singly occupied d_{xz} and d_{yz} MOs that shifts some α-spin density from the Mn ion to the O atom.[47] Both DFT and CASSCF/NEVPT2 computations complexes have also identified a low-lying ^4E electronic excited state for Mn^{IV}-oxo complexes that is characterized by a $(d_{xy})^1(d_{xz},d_{yz})^1(d_{x^2-y^2})^1(d_{z^2})^0$ configuration.[47-51] This new configuration creates a ^4E state. Importantly, this ^4E state has Mn^{III}-oxyl character, which is manifested in oppositely signed spin density on the Mn and O centers (Figure 5, right).[47-48]

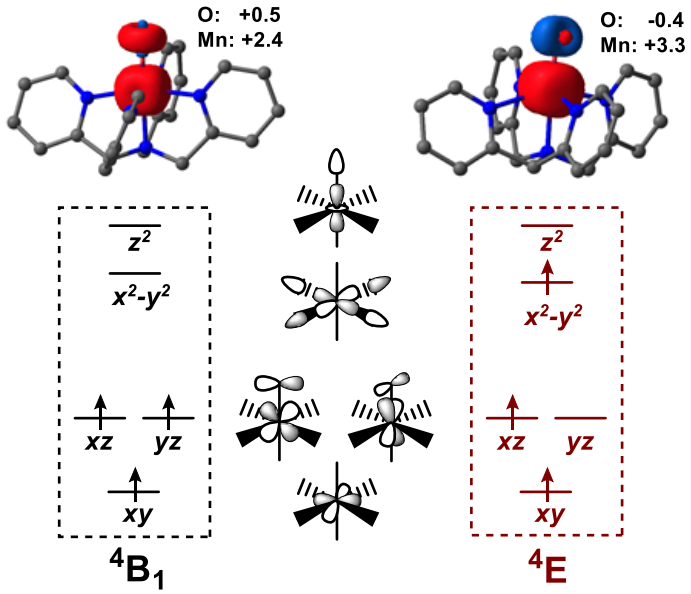

Figure 5. Electronic configurations, MO splitting patterns, and spin density plots for Mn^{IV}-oxo complexes in a six-coordinate geometry. The spin density plots are taken from CASSCF/NEVPT2 computations for a Mn^{IV}-oxo complex described in ref. [47].

The spin density in the quintet transition state of $[Mn^{III}(OO^tBu)(N_4S)]^+$ suggests that the Mn-oxo unit is similar to a Mn^{IV}-oxo species in a ^4E state, with oppositely signed spin density on the Mn and oxo units (cf. Table 1 and Figure 5). Inspection of the MOs of the quintet transition state of $[Mn^{III}(OO^tBu)(N_4S)]^+$ lends credence to this conclusion (Figures 3 and 4). This transition state has three singly occupied MOs (SOMOs) of dominant Mn d character (d_{xy}, d_{xz}, and $d_{x^2-y^2}$) and one SOMO that is an admixture of Mn d and ^{t}BuO character (O^tBu – d_{yz}). Thus, the electron configuration of the quintet transition state displays features of 1) a ^4E Mn^{IV}-oxo unit, characterized by the $(d_{xy})^1(d_{xz})^1(d_{x^2-y^2})^1(d_{yz})^0(d_{z^2})^0$ configuration, and 2) an S = ½ O^tBu radical, characterized by the singly occupied O^tBu - d_{yz} MO.

An analysis of the MOs for the triplet transition state, which shows positive spin densities on both the Mn and coordinating O atom (Table 1), reveals a $(d_{yz}$ - $O^tBu)^2(d_{xy})^1(d_{xz})^1(d_{x^2-y^2})^0(d_{z^2})^0$ configuration (Figures 3 and 4). This transition state closely resembles the more stable $^4B_1$ ground state of isolated Mn^{IV}-oxo complexes. Thus, the triplet transition state of $[Mn^{III}(OO^tBu)(N4S)]^+$

features a more stable electronic configuration for a Mn^{IV}-oxo unit, which could account for its relatively low energy.

The $[Mn^{III}(OO^tBu)(N4S)]^+$ transition states evolve to give quintet and triplet product complexes that are ~5 kcal mol^{-1} below the transition states and ~17 kcal mol^{-1} above the quintet $[Mn^{III}(OO^tBu)(N4S)]^+$ reactant (Figure 3). A calculation considering the infinitely separated products (*i.e.*, separate $[Mn^{IV}(O)(N4S)]^+$ and ^{t}BuO• species) yields a similar ΔH value of ~18 kcal mol^{-1} relative to the reactant, but a positive $T\Delta S$ term of 11 kcal mol^{-1} gives a total free energy change of only 7 kcal mol^{-1}.[52] This result is similar to calculations of O–O homolysis for low-spin Fe^{III}-alkylperoxo complexes.[18-19] In those cases, O–O cleavage was endothermic by ~15 kcal mol^{-1}, but the large entropy of reaction (~14 kcal mol^{-1}) made the free energy of reaction close to zero.

In the quintet product complex, the Mn d_{yz} and O^{t}Bu MOs that were highly mixed in the transition state (Figure 5), appear as separate MOs with essentially no mixing (Figure S1). Moreover, the Mn^{IV}-oxo unit in the quintet product complex displays the $(d_{xy})^1(d_{xz},d_{yz})^2(d_{x^2-y^2})^0(d_{z^2})^0$ configuration characteristic of the $^4B_1$ state (Figure 3 and S1), revealing that the electronic structure of the Mn-oxo unit evolves considerably from the quintet transition state to the product complex. The ^{t}BuO• radical in the quintet product carries an unpaired α-spin electron, which, when coupled with the three α-spin electrons on the Mn^{IV} center, gives the quintet state. The triplet product complex consists of a Mn^{IV}-oxo unit with a $(d_{xy})^1(d_{xz},d_{yz})^2(d_{x^2-y^2})^0(d_{z^2})^0$ configuration and a ^{t}BuO• radical with negative spin density (Table 1 and Figure 3). Thus, the product complexes consist of an S = 3/2 Mn^{IV}-oxo complex coupled ferromagnetically (quintet) or antiferromagnetically (triplet) to an S = ½ ^{t}BuO• radical.

B) Reactants, Transitions States, and Products for $[Mn^{III}(OO^tBu)(^{6Me}dpaq)]^+$. For $[Mn^{III}(OO^tBu)(^{6Me}dpaq)]^+$, the reaction begins on the quintet state, which is 8.6 kcal mol^{-1} lower

in energy than the triplet state (Figure 6 and Table 3). The quintet state arises from a Mn $(d_{xy})^1(d_{xz})(d_{yz})^1(d_{x^2-y^2})^1(d_{z^2})^0$ configuration, while in the triplet state the Mn d_{xy} MO is doubly-occupied and the Mn $d_{x^2-y^2}$ MO is unoccupied (Mn $(d_{xy})^2(d_{xz})(d_{yz})^1(d_{x^2-y^2})^0(d_{z^2})^0$ configuration; see Figure 6). The quintet-triplet energy gap for $[Mn^{III}(OO^tBu)(^{6Me}dpaq)]^+$ thus reflects 1) the spin pairing energy required to place two electrons in the Mn d_{xy} MO, and 2) the difference in energy between the Mn d_{xy} and $d_{x^2-y^2}$ MOs. Because these MOs are respectively involved in π- and σ-interactions in the equatorial plane, the energy gap will be most sensitive to perturbations in the equatorial ligand field. These calculations also reveal a distinction between the triplet states of the two Mn^{III}-alkylperoxo complexes considered in this study. While the triplet state of $[Mn^{III}(OO^tBu)(^{6Me}dpaq)]^+$ is achieved by pairing two electrons in the Mn d_{xy} MO (Figure 6), in the triplet state of $[Mn^{III}(OO^tBu)(N4S)]^+$ the Mn d_{yz} MO is doubly occupied (Figure 3). We attribute this difference to the presence of the thiolate ligand in the latter complex, which destabilizes the Mn d_{xy} MO through a strong π-interaction (Figure 3). As will be discussed below, this change in the electronic structure in the triplet state for these complexes has important consequences for the energies of the triplet transition states.

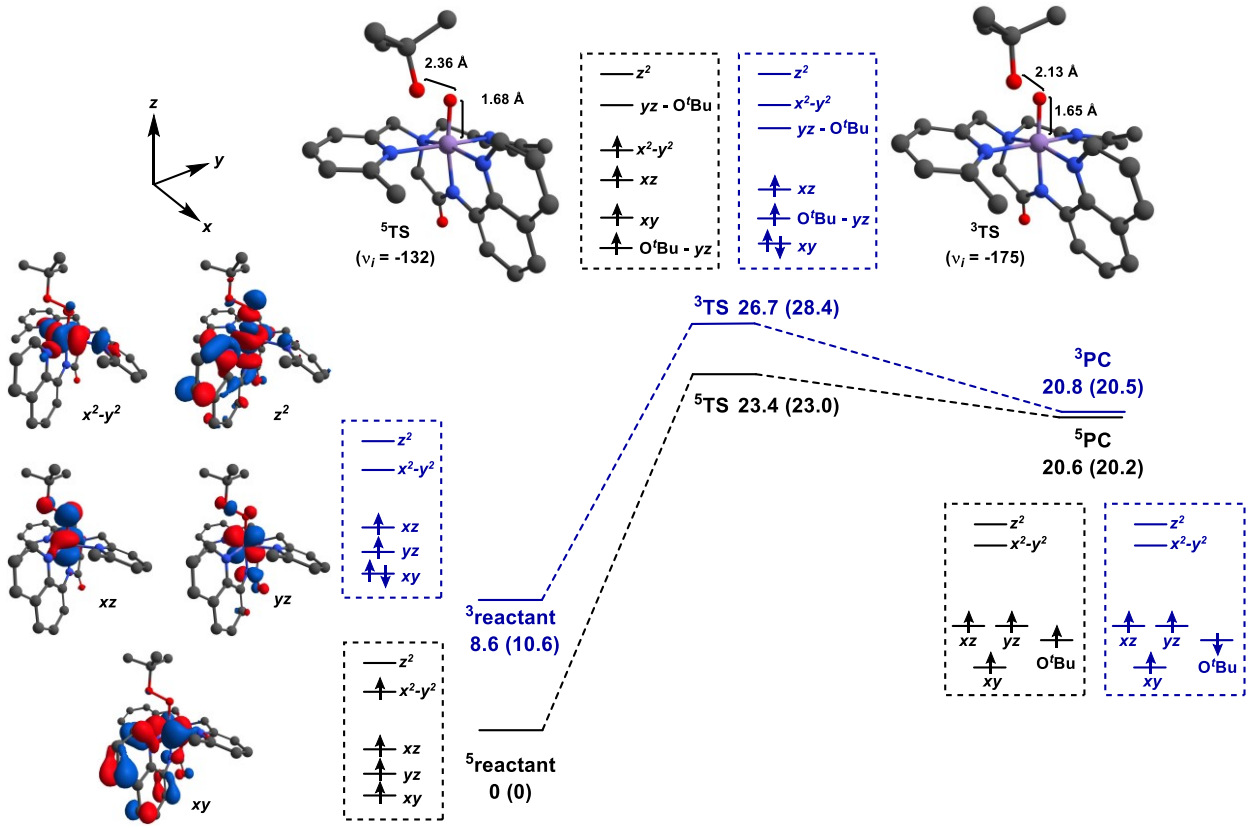

Figure 6. DFT-computed reaction coordinate for homolytic cleavage of the O–O bond of $[Mn^{III}(OO^tBu)(^{6Me}dpaq)]^+$, with structures, electronic configurations, and MO plots of key species. Enthalpies and free energies (in parentheses) are in kcal mol^{-1}.

Table 3. Selected Structural Parameters, DFT-computed Energies, and Mulliken Spin Densities for Reactants, Transition States (TS), and Product Complexes (PC) involved in the Homolytic Cleavage of the O–O Bond of $[Mn^{III}(OO^tBu)(^{6Me}dpaq)]^+$.

	^{5}reactant	^{3}reactant	^{5}TS	^{3}TS	^{5}PC	^{3}PC
structural parameters[a]						
Mn–O1	1.83	1.84	1.68	1.65	1.64	1.65
O1–O2	1.46	1.45	2.36	2.13	3.14	2.61
Mn–N1	2.04	1.98	2.02	1.99	2.00	2.00
Mn–N2	1.95	1.94	1.96	1.97	2.00	2.02
Mn–N3	2.16	2.03	2.14	2.03	2.07	2.09
Mn–N4	2.28	2.08	2.21	2.08	2.06	2.06
Mn–N5	2.40	2.12	2.47	2.15	2.53	2.47
Mn–O1–O2	108.0	113.5	102.1	111.1	93.2	101.4
N1–Mn–O1	173.6	172.4	170.7	173.8	167.3	171.5
energies[b]						
E	0	8.0	25.1	27.8	20.9	20.6
ΔH	0	8.6	23.4	26.7	20.6	20.8
$T\Delta S$	0	-2.1	0.4	-1.7	0.4	0.3
ΔG	0	10.7	23.0	28.4	20.2	20.5
spin density[c]						
Mn	3.92	1.94	3.52	1.37	2.72	2.62
O1	0.03	0.11	-0.45	-0.10	0.36	0.41
O2	0.04	0.05	0.80	0.74	0.86	-0.82

[a] Bond lengths in Å; bond angles in degrees. Atom numbering scheme is shown in Figure 1. [b] All energies in kcal mol^{-1}. The electronic energy E is taken from a single-point DFT calculation. The enthalpy (ΔH) is the sum of the electronic, zero-point, and thermal energies. The entropy term ($T\Delta S$) includes vibrational, rotational, and translational entropies is at 298 K. The free energy (ΔG) includes both the enthalpic and entropic terms.

The quintet transition-state for O–O cleavage is 23.4 kcal mol^{-1} above the quintet reactant, which is in good agreement with the experimental barrier ($\Delta H^{\ddagger}$ = 21.4 kcal mol^{-1} and $\Delta G^{\ddagger}$ = 24.2 kcal mol^{-1}; see Table 2). The structure of the transition state is shown in Figure 6 (top) and selected metric parameters are in Table 3. The transition state is quite late, as marked by a short Mn–O distance (1.68 Å) and a long O···O separation of 2.36 Å. Thus, the metric parameters in the transition state structure already resemble those of a Mn^{IV}-oxo complex. The quintet transition state of $[Mn^{III}(OO^tBu)(^{6Me}dpaq)]^+$ shows a large, positive spin density (0.80) on the non-coordinating oxygen of the OO^tBu unit (O2; see Table 3), revealing substantial ^{t}BuO• character.

The Mn-oxo unit shows an oppositely-signed spin density (Table 3), reminiscent of a Mn^{IV}-oxo species in a ^4E state (Figure 5). Overall, the electronic structure of the quintet transition state of $[Mn^{III}(OO^tBu)(^{6Me}dpaq)]^+$ is very similar to that of $[Mn^{III}(OO^tBu)(N4S)]^+$, with the former being slightly higher in energy.

The triplet transition state for $[Mn(OO^tBu)(^{6Me}dpaq)]^+$ is ~27 kcal mol^{-1} above the quintet reactant and ~4 kcal mol^{-1} higher in energy than the quintet transition state. Thus, unlike in the case of $[Mn^{III}(OO^tBu)(N4S)]^+$, the triplet transition state of $[Mn(OO^tBu)(^{6Me}dpaq)]^+$ does not offer a lower-energy pathway for O–O homolysis. This difference arises from the distinct electronic structures of the triplet states. In $[Mn(OO^tBu)(^{6Me}dpaq)]^+$, the triplet transition state has a $(d_{xy})^2(O^tBu - d_{yz})^1(d_{xz})^1(d_{yz} - O^tBu)^0(d_{x^2-y^2})^0(d_{z^2})^0$ configuration (Figures 6 and 7). The structure displays a short Mn–O1 distance of 1.65 Å and a long O1···O2 separation of 2.13 Å. Thus, the transition state is quite late and already has considerably Mn^{IV}-oxo and $^tBuO\bullet$ character. However, the Mn^{IV}-oxo unit in the triplet transition state of $[Mn(OO^tBu)(^{6Me}dpaq)]^+$ is best described as a low-spin (S = ½) Mn^{IV} center. This description is supported by the low Mn spin density of 1.4 (Table 3). In contrast, the triplet transition state of $[Mn(OO^tBu)(N4S)]^+$ has a high-spin (S = 3/2) Mn^{IV} center characterized by a Mn spin density of 2.22 (Table 1). This significant difference in spin density arises because of the distinct ordering of the Mn d_{xy} and $O^tBu - d_{yz}$ MOs for these transition states. In the $[Mn(OO^tBu)(N4S)]^+$ complex, the strong Mn-thiolate π-antibonding interaction in the Mn d_{xy} MO pushes this orbital above the $O^tBu - d_{yz}$ MO, leading to the $(O^tBu - d_{yz})^2(d_{xy})^1(d_{xz})^1(d_{yz} - O^tBu)^0(d_{x^2-y^2})^0(d_{z^2})^0$ configuration. In contrast, the Mn d_{xy} MO in $[Mn(OO^tBu)(^{6Me}dpaq)]^+$ lacks a similarly strong antibonding interaction, and this MO lies below the $O^tBu - d_{yz}$ MO. Consequently, the $[Mn(OO^tBu)(^{6Me}dpaq)]^+$ complex has the $(d_{xy})^2(O^tBu -$

$d_{yz})^1(d_{xz})^1(d_{yz}$ - O^{t}Bu$)^0(d_{x^2-y^2})^0(d_{z^2})^0$ configuration, where the double occupancy of the Mn d_{xy} MO leads to the low-spin Mn center, which increases the energy of the triplet transition state.

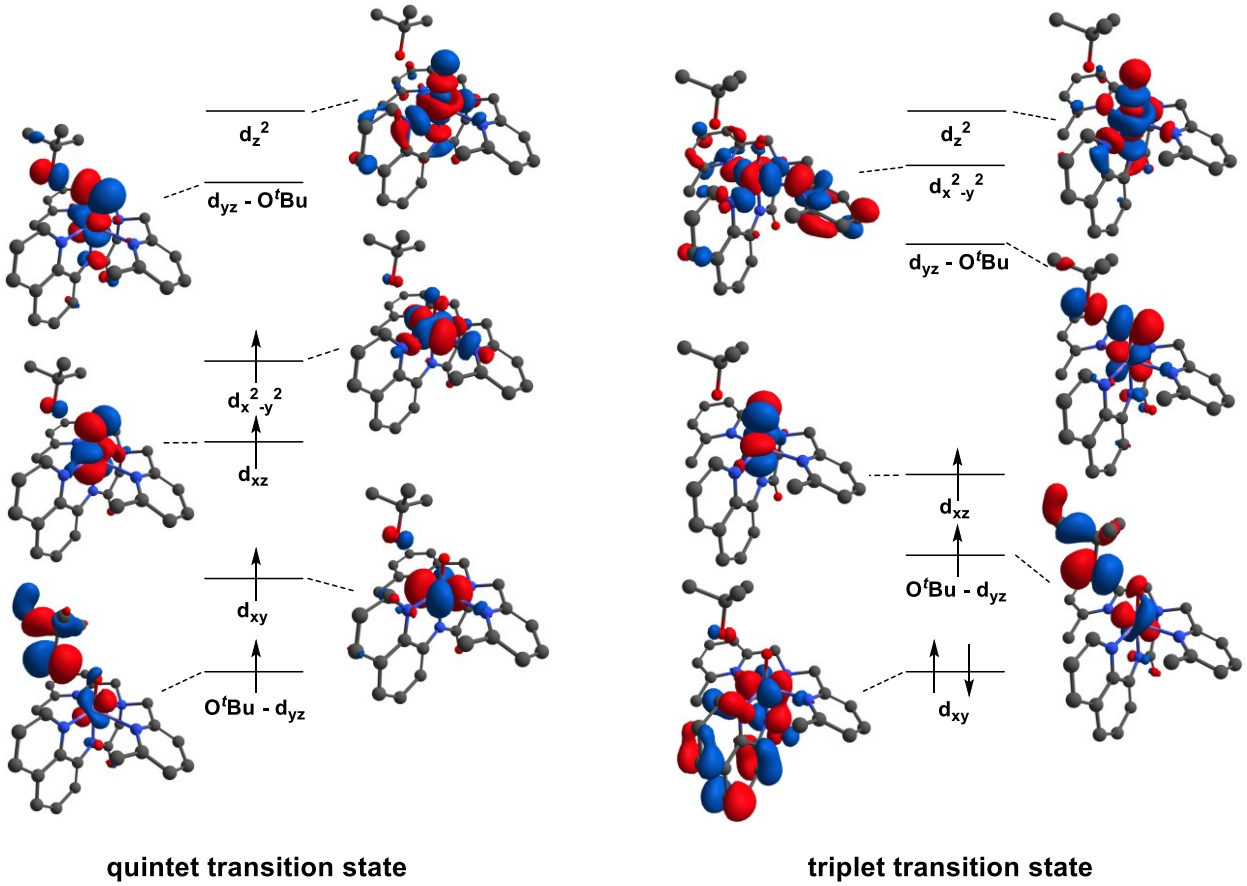

Figure 7. Surface contour plots and qualitative frontier MO splitting diagrams for the quintet (left) and triplet (right) transition states of $[Mn^{III}(OO^tBu)(^{6Me}dpaq)]^+$.

Heterolytic Cleavage of the O–O Bond. The thermal decay of $[Mn^{III}(OOCm)(N4S)]^+$ exclusively yields acetophenone, which is the expected product of O–O homolysis.[27, 53] In contrast, the decay of $[Mn^{III}(OOCm)(^{6Me}dpaq)]^+$ yields products of both O–O homolysis and heterolysis.[30] To explore the basis for this difference, we investigated pathways for heterolytic cleavage of the O–O bond for these complexes on the single surface.

A) Singlet Reactants, Transitions States, and Products for $[Mn^{III}(OO^tBu)(N4S)]^+$. The singlet state of $[Mn^{III}(OO^tBu)(N4S)]^+$ lies ~20 kcal mol^{-1} above the quintet state (Figure 8). This

singlet state is characterized by a low-spin Mn^{III} center, with a $(d_{yz})^2(d_{xy})^2(d_{xz})^0(d_{x^2-y^2})^0(d_{z^2})^0$ configuration. The lack of electrons in the σ-antibonding MOs ($d_{x^2-y^2}$ and d_{z^2}) leads to short Mn–N distances (Table 4). In particular the Mn–N3 and Mn–N4 bond lengths, which involve the 6-Me-pyridyl groups, contract significantly by ~0.2 – 0.3 Å relative to the quintet $[Mn^{III}(OO^tBu)(N4S)]^+$ complex. The Mn–O1 and O1–O2 bonds are only slightly perturbed (Table 4).

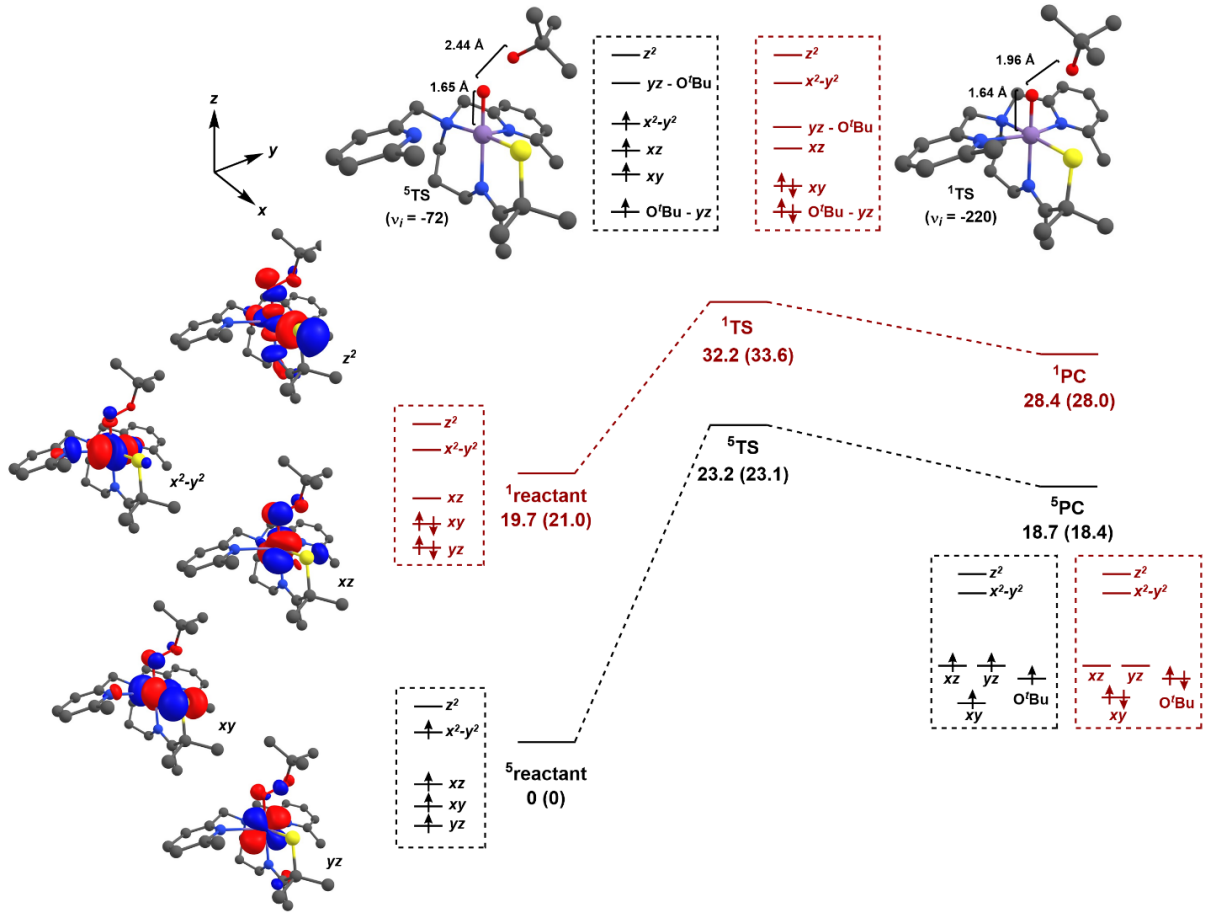

Figure 8. DFT-computed reaction coordinate for O–O bond cleavage for $[Mn^{III}(OO^tBu)(N4S)]^+$ on the quintet and singlet surfaces, with structures, electronic configurations, and MO plots of key species. Enthalpies and free energies (in parentheses) are in kcal mol^{-1}.

Table 4. Selected Structural Parameters, DFT-computed Energies, and Mulliken Spin Densities for Reactants, Transition States (TS), and Product Complexes (PC) involved in the Heterolytic Cleavage of the O–O Bond of $[Mn^{III}(OO^tBu)(N4S)]^+$.

	^{5}reactant	^{1}reactant	^{1}TS	^{1}PC
structural parameters[a]				
Mn–O1	1.84	1.81	1.64	1.61
O1–O2	1.45	1.45	1.96	2.88
Mn–S1	2.25	2.24	2.24	2.25
Mn–N1	2.09	2.11	2.21	2.22
Mn–N2	2.22	2.15	2.14	2.12
Mn–N3	2.50	2.21	2.13	2.10
Mn–N4	2.43	2.23	2.21	2.25
Mn–O1–O2	110.0	112.7	116.7	134.2
N1–Mn–O1	174.8	174.1	174.4	174.7
energies[b]				
E	0	20.9	32.8	30.6
ΔH	0	19.7	32.2	28.4
$T\Delta S$	0	-1.3	-1.4	0.4
ΔG	0	21.0	33.6	28.0

[a] Bond lengths in Å; bond angles in degrees. Atom numbering scheme is shown in Figure 1. [b] All energies in kcal mol^{-1}. The electronic energy E is taken from a single-point DFT calculation. The enthalpy (ΔH) is the sum of the electronic, zero-point, and thermal energies. The entropy term ($T\Delta S$) includes vibrational, rotational, and translational entropies is at 298 K. The free energy (ΔG) includes both the enthalpic and entropic terms.

The singlet transition state of $[Mn^{III}(OO^tBu)(N4S)]^+$ is quite high in energy, lying ~10 kcal mol^{-1} above the quintet *and* triplet transition states (cf. Figures 8 and 3). The high energy of this transition state relative to other paths is in excellent agreement with the lack of O–O heterolysis products observed in the decay of $[Mn^{III}(OOCm)(N4S)]^+$.[26] An examination of the frontier MOs of the singlet transition state shows two electrons in the Mn d_{xy} MO and two electrons in an MO that is mixed between the ^{t}BuO group and the Mn d_{yz} orbital (Figure S2). The transition state structure consists of a short Mn–O bond (1.64 Å) and an elongated O–O distance (1.96 Å). The singlet product complex is also at quite high of an energy (28.4 kcal mol^{-1} relative to the quintet reactant). This product is well described by an $S = 0$ Mn^V-oxo unit and a ^{t}BuO$^-$ anion (Figure 8).

Thus, the energies of all singlet species for $[Mn^{III}(OO^tBu)(N4S)]^+$ are high above the corresponding quintet and triplet species, demonstrating that O–O heterolysis is an unfavorable decay pathway for this complex.

B) Singlet Reactants, Transitions States, and Products for $[Mn^{III}(OO^tBu)(^{6Me}dpaq)]^+$. The singlet state of $[Mn^{III}(OO^{t}Bu)(^{6Me}dpaq)]^+$ is ~17 kcal mol^{-1} above the quintet ground state and has a low-spin Mn^{III} center with a $(d_{xy})^2(d_{yz})^2(d_{xz})^0(d_{x^2-y^2})^0(d_{z^2})^0$ configuration (Figure 9). The unoccupied Mn $d_{x^2-y^2}$ MO in the singlet state leads to equatorial Mn–N bonds that are contracted by ~0.13 – 0.28 Å relative to the quintet ground state (Table 5). The singlet transition state for $[Mn^{III}(OO^{t}Bu)(^{6Me}dpaq)]^+$ lies ~26 kcal mol^{-1} above the quintet ground state, which is only ~3 kcal mol^{-1} higher in energy than the quintet transition state (Figure 9). Thus, the gap between the quintet and singlet transition states for $[Mn^{III}(OO^tBu)(^{6Me}dpaq)]^+$ (~3 kcal mol^{-1}) is much smaller than the corresponding gap predicted for $[Mn^{III}(OO^tBu)(N4S)]^+$ (~10 kcal mol^{-1}; see Figure 8). This prediction is in accordance with the observation of both homolysis and heterolysis O–O cleavage products upon thermal decay of the $[Mn^{III}(OOCm)(^{6Me}dpaq)]^+$ complex.[30]

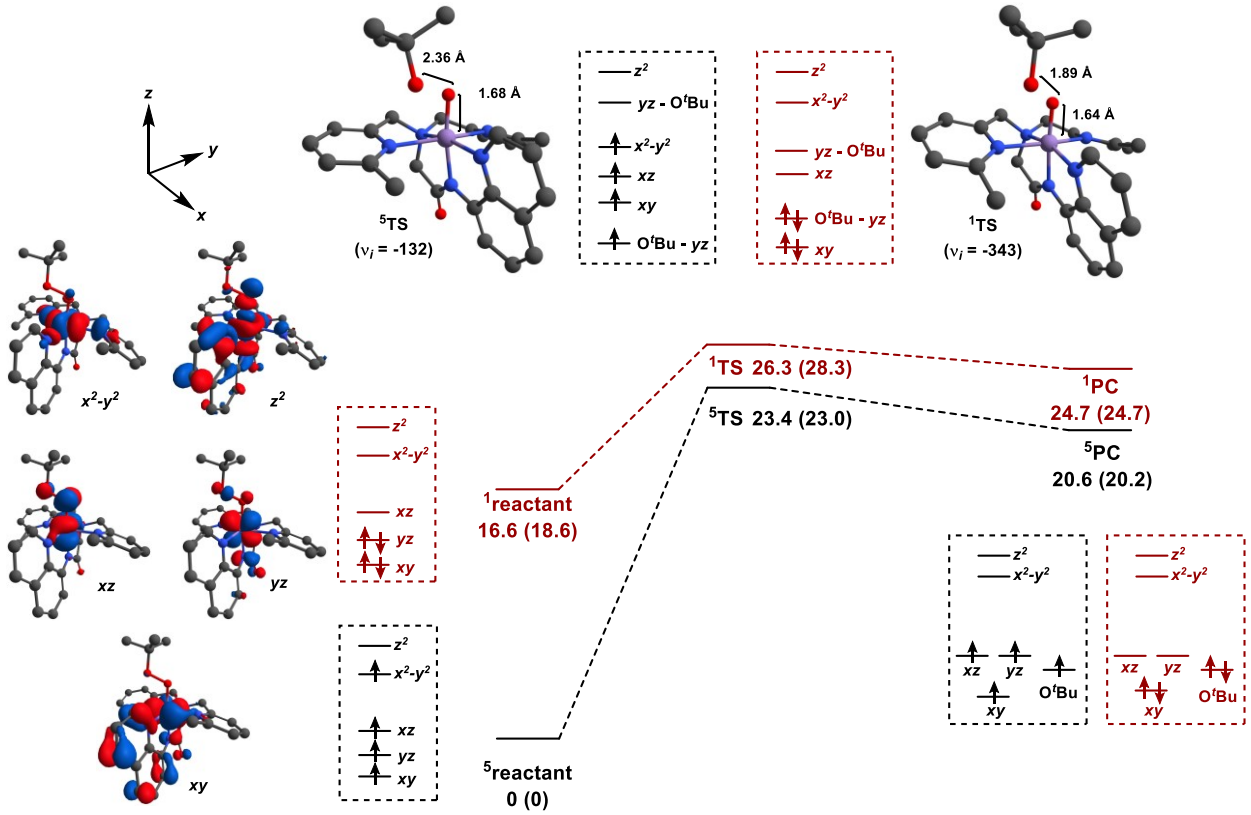

Figure 9. DFT-computed reaction coordinate for O–O bond cleavage for $[Mn^{III}(OO^tBu)(^{6Me}dpaq)]^+$ on the quintet and singlet surfaces, with structures, electronic configurations, and MO plots of key species. Enthalpies and free energies (in parentheses) are in kcal mol^{-1}.

The structure of the singlet transition state for $[Mn^{III}(OO^tBu)(^{6Me}dpaq)]^+$ shows a short Mn–O1 distance of 1.64 Å, consistent with multiple bond character. The O1–O2 bond has elongated to 1.89 Å, while all Mn–N distances are similar to those in the singlet reactant (Table 5). The lack of change in Mn–N distances from the singlet reactant to transition state stands in contrast to that observed for $[Mn^{III}(OO^tBu)(N4S)]^+$, where the Mn–N1 and Mn–N3 distances elongate and contract, respectively (Table 4). The frontier MOs in the singlet transition state of $[Mn^{III}(OO^tBu)(^{6Me}dpaq)]^+$ consist of a doubly-occupied Mn d_{xy} MO and an MO delocalized between the Mn d_{yz} orbital and the alkylperoxo unit (Figure S2). The singlet transition state of $[Mn^{III}(OO^tBu)(^{6Me}dpaq)]^+$ evolves to the singlet product complex, which lies 24.7 kcal mol^{-1} above

the quintet reactant (Figure 9). This product consists of an $S = 0$ Mn^{V}-oxo species and a $^{t}BuO^{-}$ anion.

Table 5. Selected Structural Parameters, DFT-computed Energies, and Mulliken Spin Densities for Reactants, Transition States (TS), and Product Complexes (PC) involved in the Heterolytic Cleavage of the O–O Bond of $[Mn^{III}(OO^{t}Bu)(^{6Me}dpaq)]^{+}$.

	^{5}reactant	^{1}reactant	^{1}TS	^{1}PC
structural parameters[a]				
Mn–O1	1.83	1.81	1.64	1.60
O1–O2	1.46	1.45	1.89	3.18
Mn–N1	2.04	1.99	1.98	2.00
Mn–N2	1.95	1.96	1.99	2.00
Mn–N3	2.16	2.03	2.04	2.11
Mn–N4	2.28	2.09	2.10	2.08
Mn–N5	2.40	2.12	2.12	2.46
Mn–O1–O2	108.0	116.7	114.7	96.0
N1–Mn–O1	173.6	172.2	173.0	168.0
energies[b]				
E	0	16.1	27.2	24.1
ΔH	0	16.6	26.3	24.7
$T\Delta S$	0	-1.9	-2.0	0.03
ΔG	0	18.6	28.3	24.7

[a] Bond lengths in Å; bond angles in degrees. Atom numbering scheme is shown in Figure 1. [b] All energies in kcal mol^{-1}. The electronic energy E is taken from a single-point DFT calculation. The enthalpy (ΔH) is the sum of the electronic, zero-point, and thermal energies. The entropy term ($T\Delta S$) includes vibrational, rotational, and translational entropies is at 298 K. The free energy (ΔG) includes both the enthalpic and entropic terms.

Discussion.

Electronic Factors that Control the Stability of Mn^{III}-alkylperoxo Complexes. Experimental investigations of the decay rates of Mn^{III}-alkylperoxo complexes have identified two important factors that affect these rates: 1) Mn–N bond elongations *cis* to the alkylperoxo ligand, and 2) thiolate versus non-thiolate coordination. A series of crystallographic and kinetic studies of Mn^{III}-alkylperoxo complexes supported by N4S ligands revealed that longer Mn–N distances *cis* to the alkylperoxo ligand give rise to shorter O–O bonds. These shorter O–O bonds correlated with

slower thermal decay rates for O–O homolysis (Figure 10).[26] This correlation was attributed to changes in the Lewis acidity of the Mn center as a function of the Mn–N distances. Longer Mn–N distances increase the Mn Lewis acidity, enhancing charge donation from the alkylperoxo O–O π^* orbital to a Mn 3d orbital. The increased donation from the O–O π^* orbital strengthens and stabilizes the peroxo bond, rationalizing the increased stability of Mn^{III}-alkylperoxo complexes with longer Mn–N distances. While this correlation provides an elegant explanation for the trend in decay rates of thiolate-ligated Mn^{III}-alkylperoxo complexes, its application to complexes lacking thiolate ligands is less robust (Figure 10). For example, the crystal structure of $[Mn^{III}(OOCm)(^{6Me}dpaq)]^+$ reveals an O–O bond length on the longer end of the series (1.466(4) Å), but this complex is stable at room temperature ($t_{1/2} \approx 5$ days).[30] For comparison, the $[Mn^{III}(OOR)(N4S)]^+$ complexes have half-lives of less than 5 minutes at 20 °C.[26] Moreover, an alkoxide-ligated $[Mn^{III}(OOR)(N4O)]^+$ complex also has a long O–O bond (1.473(1) Å) and is stable at room temperature ($t_{1/2} \approx 2$ hours).[28] Thus, longer O–O bonds are not always associated with faster decay. Nonetheless, in both of the complexes lacking thiolate ligation, DFT computations revealed greater Lewis acidity for the Mn centers (as assessed by the Mulliken charges),[28, 30] which could foster increased alkylperoxo-to-manganese(III) charge donation. It is unclear why potentially greater charge donation in those cases did not lead to shorter O–O distances.

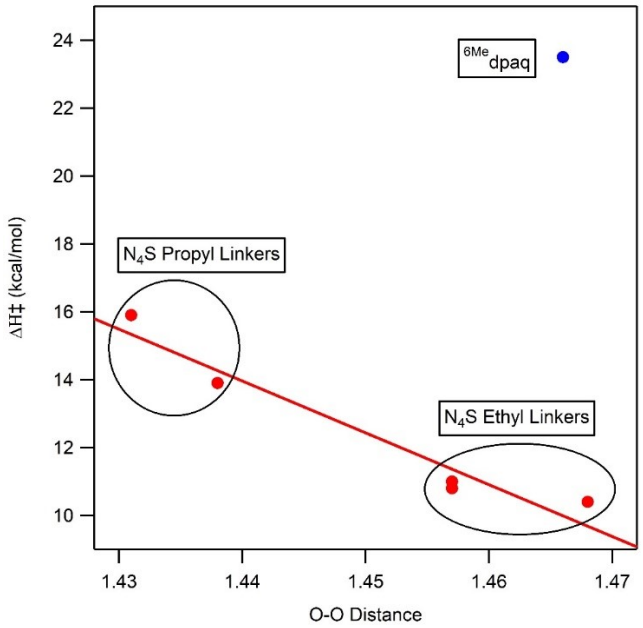

Figure 10. Comparison of thermal decay rates and structural parameters for Mn^{III}-alkylperoxo complexes supported by a range of ligands. Data from references [26] and [30].

Our computations offer a complementary explanation for the trend in the decay rates of the $[Mn^{III}(OOR)(N4S)]^+$ complexes *and* provide insight into the remarkable stability of the $[Mn^{III}(OOR)(^{6Me}dpaq)]^+$ and $[Mn^{III}(OOR)(N4O)]^+$ complexes. Considering first the $[Mn^{III}(OO^tBu)(N4S)]^+$ series, our computations suggest that O–O homolysis could occur by a two-state mechanism, where the quintet reactant crosses to a triplet surface along the reaction coordinate (Figure 3). According to this model, the stability of a $[Mn^{III}(OOR)(N4S)]^+$ complex would then be affected by the quintet-triplet gap. Complexes with lower-lying triplet states should have lower barriers for O–O homolysis. For the $[Mn^{III}(OO^tBu)(N4S)]^+$ series, the variation in Mn–N distances in the equatorial plane should directly influence the quintet-triplet gap. Longer Mn–N distances should stabilize the Mn $d_{x^2-y^2}$ MO, while only modestly affecting the energies of other Mn 3d orbitals. A lower-energy Mn $d_{x^2-y^2}$ MO should stabilize the quintet ground state relative to that of the triplet excited state, thereby increasing the quintet-triplet gap. This model is thus consistent with the trend that longer equatorial Mn–N bond lengths stabilize Mn^{III}-

alkylperoxo complexes. The weak equatorial fields increase the quintet-triplet gap, thereby disfavoring O–O homolysis on the triplet spin surface.

The DFT computations for $[Mn^{III}(OO^tBu)(^{6Me}dpaq)]^+$ also offer an explanation for why this complex and $[Mn^{III}(OOCm)(^{6Me}dpaq)]^+$ do not follow the structure-reactivity trend for the $[Mn^{III}(OOR)(N4S)]^+$ complexes. The triplet transition state for the $[Mn^{III}(OOR)(N4S)]^+$ complex has a $(d_{yz}$ - $O^tBu)^2(d_{xy})^1(d_{xz})^1(d_{x^2-y^2})^0(d_{z^2})^0$ configuration (Figure 11, left). This transition state is stabilized because the doubly-occupied MO contains an admixture of Mn d_{yz} and alkylperoxo O–O σ* character (Figure 11, bottom left). As discussed for Fe^{III}-alkylperoxo complexes,[18-19] O–O bond cleavage requires transfer of electron density from the metal center to the alkylperoxo σ* MO. The doubly-occupied O^tBu – d_{yz} MO in the triplet state of $[Mn^{III}(OOR)(N4S)]^+$ nicely facilitates this charge transfer. In contrast, the triplet transition state of $[Mn^{III}(OO^tBu)(^{6Me}dpaq)]^+$ has a $(d_{xy})^2(d_{yz}$ - $O^tBu)^1(d_{xz})^1(d_{x^2-y^2})^0(d_{z^2})^0$ configuration, which leads to an unfavorable low-spin Mn^{IV} center in the transition state (Figure 11, right). Consequently, the triplet transition state for $[Mn^{III}(OO^tBu)(^{6Me}dpaq)]^+$ is higher in energy than the quintet transition state (Figure 6) and this complex does not follow a two-state reactivity model.

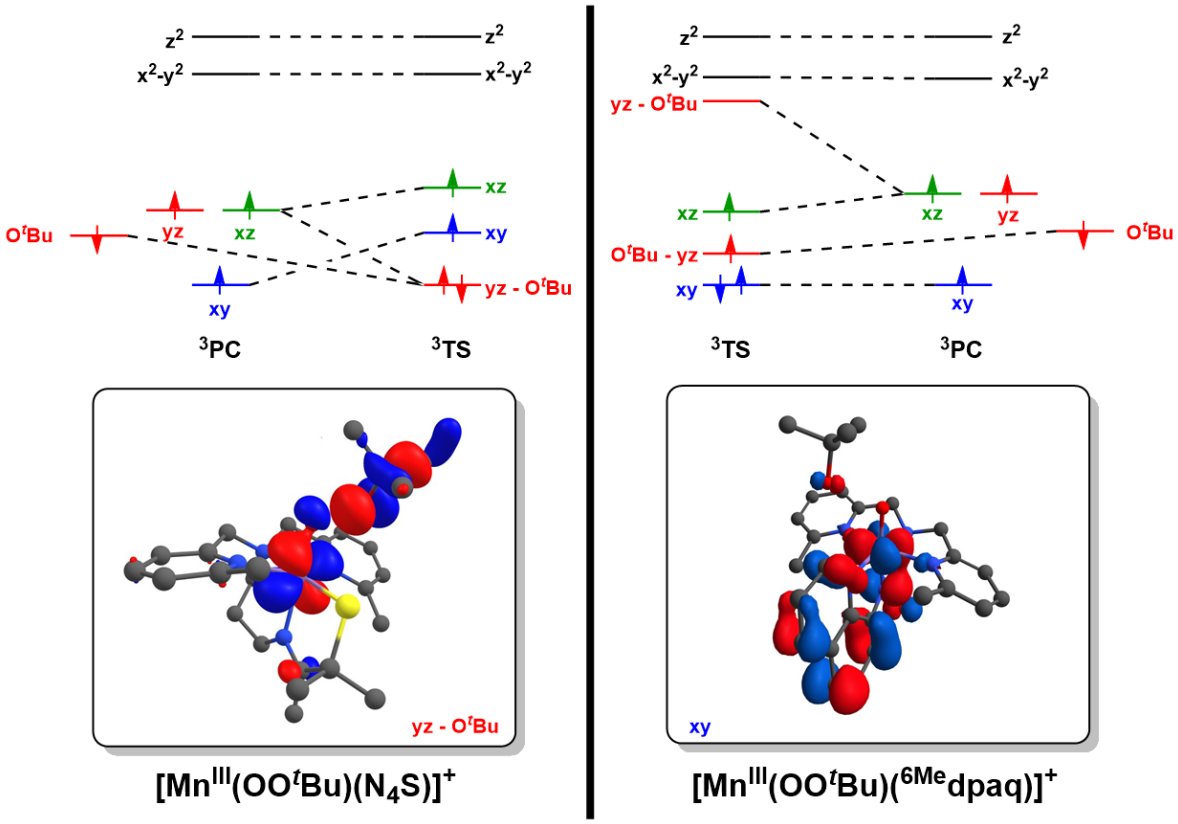

Figure 11. Electronic configurations showing the conversion of the triplet spin $[Mn^{III}(OO^tBu)(N4S)]^+$ (left) and $[Mn^{III}(OO^tBu)(^{6Me}dpaq)]^+$ transition states to the O–O bond homolysis products (top). Surface contour plots of the doubly-occupied MOs in the triplet transition states are included (bottom).

The different configurations of the triplet transition states of $[Mn^{III}(OOR)(N4S)]^+$ and $[Mn^{III}(OO^tBu)(^{6Me}dpaq)]^+$ can be linked to the presence of the thiolate ligand in the former complex. The thiolate has a strong π-interaction with the Mn d_{xy} orbital, destabilizing this MO such that it lies above the Mn d_{yz} MO (Figures 3 and 4). In contrast, the Mn d_{xy} MO of $[Mn^{III}(OO^tBu)(^{6Me}dpaq)]^+$ is essentially non-bonding and therefore is the lowest-energy Mn d orbital (Figures 6 and 7). We propose that a similar explanation can account for the high stability of the alkoxide-containing $[Mn^{III}(OO^tBu)(N4O)]^+$ complex. The alkoxide ligand is a weaker π-donor than a thiolate and, therefore, the triplet transition state for $[Mn^{III}(OO^tBu)(N4O)]^+$ should have an electronic structure similar to that of $[Mn^{III}(OO^tBu)(^{6Me}dpaq)]^+$ (Figure 11, right).

O-O Homolysis versus Heterolysis. Previous studies have revealed subtle, albeit important, differences in the thermal decay pathways of Mn^{III}-cumylperoxo complexes of the N4S and ^{6Me}dpaq ligands. The decay of $[Mn^{III}(OOCm)(N4S)]^+$ complexes revealed exclusive formation of acetophenone (68 – 72% yield), with no observed cumyl alcohol.[26] This distribution of decay products suggests that O–O homolysis is the dominant decay pathway (generating acetophenone by β-scission of a cumyloxyl radical). In contrast, the decay of $[Mn^{III}(OOCm)(^{6Me}dpaq)]^+$ revealed a mixture of acetophenone and cumyl alcohol (70 and 30%, respectively, in benzonitrile),[30] suggestive of decay by both O–O homolysis and heterolysis pathways.

The DFT computations described here offer an appealing basis on which to rationalize these differences. As shown in Figure 8 and Table 4, all singlet states of $[Mn^{III}(OO^tBu)(N4S)]^+$ are at very high energies. For example, the singlet reactant lies 20 kcal mol^{-1} above the quintet reactant; the singlet transition state is at an even higher energy of ~32 kcal mol^{-1}. Thus, heterolysis does not occur for $[Mn^{III}(OO^tBu)(N4S)]^+$ because this step has too high a barrier relative to homolysis. This result accords nicely with the lack of O–O heterolysis products observed in experimental studies of the decay of $[Mn^{III}(OOCm)(N4S)]^+$.[26-27] The high energy of these low-spin states is attributed to the presence of the weak field thiolate ligand, which destabilizes one of the doubly-occupied MOs in the singlet state.

In contrast, all singlet states for $[Mn (OO^tBu)(^{6Me}dpaq)]^+$ are at lower energies (Figure 9 and Table 5). Most significantly, the singlet transition state of $[Mn(OO^tBu)(^{6Me}dpaq)]^+$ is only ~3 kcal mol^{-1} higher in energy than the quintet transition state, suggesting that both transition states might be accessed during thermal decay. Accordingly, this smaller singlet-quintet gap for $[Mn^{III}(OO^tBu)(^{6Me}dpaq)]^+$ is in agreement with the observation of both homolysis and heterolysis products in the thermal decay of $[Mn^{III}(OOCm)(^{6Me}dpaq)]^+$.[30]

The relative energies of these various transition states have large consequences on controlling O–O heterolysis and homolysis pathways and therefore are highly pertinent for Mn catalysts that activate alkyl- and hydro-peroxides. For these catalysts, O–O heterolysis is the preferred path, as it yields a more reactive Mn^{V}-oxo species and does not produce RO• radials, the latter of which are undesirable as they can promote non-specific oxidation reactions. Our computations suggest that the singlet state, and thus O–O heterolysis, can be favored by the lack of equatorial ligands that are good π-donors. Indeed, most Mn catalysts that are effective at activating H_2O_2 contain nitrogen-based ligands that have intermediate ligand field strengths.[1-5]

Finally, it is important to note that our present computations do not probe the role of acid in stabilizing various O–O cleavage transition states. However, our previous experiments investigating the reaction of $[Mn^{III}(OOCm)(^{6Me}dpaq)]^{+}$ with PPh_3 revealed exclusive formation of cumyl alcohol in this reaction.[30] This result suggested that PPh_3 altered the O–O cleavage pathway to foster O–O heterolysis. Future experimental and computational studies will explore the role of electrophiles such as PPh_3 and Lewis acids such as H^{+} in influencing O–O decay mechanisms.

Conclusions.

In this present work, we have used DFT computations to compare the O–O activation pathways of $[Mn^{III}(OO^{t}Bu)(N4S)]^{+}$ and $[Mn^{III}(OO^{t}Bu)(^{6Me}dpaq)]^{+}$. Previous experimental studies of these complexes had revealed intriguing differences between stabilities and decay pathways.[26, 30] Our computations suggest that the relative energies of transition states with different spin multiplicities contribute to the different decay properties of these complexes. For example, the high energy of all singlet species for $[Mn^{III}(OO^{t}Bu)(N4S)]^{+}$ discourages O–O heterolysis (Figure 8). This result helps rationalize the lack of observed heterolysis products in experimental studies of the decay of

the corresponding Mn^{III}-OOCm complex.[26-27] Intriguingly, the computations indicate that several Mn^{IV}-oxo units can be generated in the transition state. On the quintet surface, both complexes form Mn^{IV}-oxo units with excited ^4E configurations. Given that the ^4E state of Mn^{IV}-oxo complexes have been predicted to be quite reactive, decay pathways involving this state could yield potent oxidants. In contrast, on the triplet surface, different Mn^{IV}-oxo species are calculated in the transition states of the $[Mn^{III}(OO^tBu)(N4S)]^+$ and $[Mn^{III}(OO^tBu)(^{6Me}dpaq)]^+$ complexes. The former contains a favorable $S = 3/2$ Mn^{IV}-oxo unit, while the latter has an unusual, low-spin $S = ½$ Mn^{IV}-oxo species. These different electronic structures contribute to the difference in energy of these transition states. For $[Mn^{III}(OO^tBu)(N4S)]^+$, the low energy of the triplet transition state renders it possible that O–O homolysis occurs by a two-state mechanism, where the system crosses from the initial quintet state to a triplet state. In contrast, the triplet transition state of $[Mn^{III}(OO^tBu)(^{6Me}dpaq)]^+$ is at too high of an energy relative to the quintet transition state to allow for a two-state mechanism for O–O homolysis.

Author contributions

All authors conceived, planned, and performed the computations and contributed to data analysis. S.A.B. and T.A.J. wrote the manuscript.

Conflicts of Interest

There are no conflicts to declare.

Acknowledgements

This work was supported by the U.S. National Science Foundation (CHE-2154955 to T. A. J.).

The calculations were performed at the University of Kansas Center for Research Computing (CRC), including the BigJay Cluster resource funded through U.S. NSF Grant MRI-2117449.

Table of Contents Entry

Through the use of density functional theory calculations and comparisons with published experimental data, the differences in the decay pathways of the Mn^{III}-alkylperoxo complexes $[Mn^{III}(OO^tBu)(^{6Me}dpaq)]^+$ and $[Mn^{III}(OO^tBu)(N4S)]^+$ are rationalized.

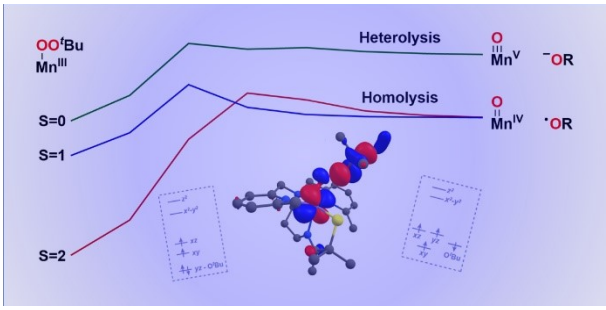

References.

1. Chen, J.; Jiang, Z.; Fukuzumi, S.; Nam, W.; Wang, B., Artificial nonheme iron and manganese oxygenases for enantioselective olefin epoxidation and alkane hydroxylation reactions. *Coord. Chem. Rev.* **2020,** *421*, 213443.
2. Sun, W.; Sun, Q., Bioinspired Manganese and Iron Complexes for Enantioselective Oxidation Reactions: Ligand Design, Catalytic Activity, and Beyond. *Acc. Chem. Res.* **2019,** *52* (8), 2370-2381.
3. Vicens, L.; Olivo, G.; Costas, M., Rational Design of Bioinspired Catalysts for Selective Oxidations. *ACS Catalysis* **2020,** *10* (15), 8611-8631.
4. Aneeja, T.; Neetha, M.; Afsina, C. M. A.; Anilkumar, G., Recent advances and perspectives in manganese-catalyzed C–H activation. *Catalysis Science & Technology* **2021,** *11* (2), 444-458.
5. Philip, R. M.; Radhika, S.; Abdulla, C. M. A.; Anilkumar, G., Recent Trends and Prospects in Homogeneous Manganese-Catalysed Epoxidation. *Adv. Synth. Catal.* **2021,** *363* (5), 1272-1289.
6. Ottenbacher, R. V.; Talsi, E. P.; Rybalova, T. V.; Bryliakov, K. P., Enantioselective Benzylic Hydroxylation of Arylalkanes with H_2O_2 in Fluorinated Alcohols in the Presence of Chiral Mn Aminopyridine Complexes. *ChemCatChem* **2018,** *10* (22), 5323-5330.
7. Talsi, E. P.; Bryliakov, K. P., Chemo- and stereoselective CH oxidations and epoxidations/cis-dihydroxylations with H_2O_2, catalyzed by non-heme iron and manganese complexes. *Coord. Chem. Rev.* **2012,** *256* (13–14), 1418-1434.

8. Kasper, J. B.; Vicens, L.; de Roo, C. M.; Hage, R.; Costas, M.; Browne, W. R., Reversible Deactivation of Manganese Catalysts in Alkene Oxidation and H2O2 Disproportionation. *ACS Catalysis* **2023,** *13* (9), 6403-6415.
9. Ottenbacher, R. V.; Talsi, E. P.; Bryliakov, K. P., Chiral Manganese Aminopyridine Complexes: the Versatile Catalysts of Chemo- and Stereoselective Oxidations with H2O2. *The Chemical Record* **2018,** *18* (1), 78-90.
10. Bullock, R. M.; Chen, J. G.; Gagliardi, L.; Chirik, P. J.; Farha, O. K.; Hendon, C. H.; Jones, C. W.; Keith, J. A.; Klosin, J.; Minteer, S. D.; Morris, R. H.; Radosevich, A. T.; Rauchfuss, T. B.; Strotman, N. A.; Vojvodic, A.; Ward, T. R.; Yang, J. Y.; Surendranath, Y., Using nature's blueprint to expand catalysis with Earth-abundant metals. *Science* **2020,** *369* (6505), eabc3183.
11. Nandy, A.; Adamji, H.; Kastner, D. W.; Vennelakanti, V.; Nazemi, A.; Liu, M.; Kulik, H. J., Using Computational Chemistry To Reveal Nature's Blueprints for Single-Site Catalysis of C–H Activation. *ACS Catalysis* **2022,** *12* (15), 9281-9306.
12. Chen, J.; Song, W.; Yao, J.; Wu, Z.; Lee, Y.-M.; Wang, Y.; Nam, W.; Wang, B., Hydrogen Bonding-Assisted and Nonheme Manganese-Catalyzed Remote Hydroxylation of C–H Bonds in Nitrogen-Containing Molecules. *J. Am. Chem. Soc.* **2023,** *145* (9), 5456-5466.
13. Leto, D. F.; Jackson, T. A., Peroxomanganese complexes as an aid to understanding redox-active manganese enzymes. *J. Biol. Inorg. Chem.* **2014,** *19* (1), 1-15.
14. Sankaralingam, M.; Lee, Y.-M.; Jeon, S. H.; Seo, M. S.; Cho, K.-B.; Nam, W., A mononuclear manganese(iii)–hydroperoxo complex: synthesis by activating dioxygen and reactivity in electrophilic and nucleophilic reactions. *Chem. Commun.* **2018,** *54* (10), 1209-1212.
15. So, H.; Park, Y. J.; Cho, K.-B.; Lee, Y.-M.; Seo, M. S.; Cho, J.; Sarangi, R.; Nam, W., Spectroscopic Characterization and Reactivity Studies of a Mononuclear Nonheme Mn(III)-Hydroperoxo Complex. *J. Am. Chem. Soc.* **2014,** *136*, 12229-12232.
16. Lin, Y.-H.; Kutin, Y.; van Gastel, M.; Bill, E.; Schnegg, A.; Ye, S.; Lee, W.-Z., A Manganese(IV)-Hydroperoxo Intermediate Generated by Protonation of the Corresponding Manganese(III)-Superoxo Complex. *J. Am. Chem. Soc.* **2020,** *142* (23), 10255-10260.
17. Tian, Y.-C.; Jiang, Y.; Lin, Y.-H.; Zhang, P.; Wang, C.-C.; Ye, S.; Lee, W.-Z., Hydrogen Atom Transfer Thermodynamics of Homologous Co(III)- and Mn(III)-Superoxo Complexes: The Effect of the Metal Spin State. *JACS Au* **2022,** *2* (8), 1899-1909.
18. Lehnert, N.; Ho, R. Y. N.; Que, L. J.; Solomon, E. I., Spectroscopic Properties and Electronic Structure of Low-Spin Fe(III)-Alklyperoxo Complexes: Homolytic Cleavage of the O-O Bond. *J. Am. Chem. Soc.* **2001,** *123*, 8271-8290.
19. Lehnert, N.; Ho, R. Y. N.; Que, L. J.; Solomon, E. I., Electronic Structure of High-Spin Iron(III)-Alkylperoxo Complexes and Its Relation to Low-Spin Analogues: Reaction Coordinate of O-O Bond Homolysis. *J. Am. Chem. Soc.* **2001,** *123*, 12802-12816.
20. Costas, M.; Mehn, M. P.; Jensen, M. P.; Que, L., Jr., Dioxygen Activation at Mononuclear Nonheme Iron Active Sites: Enzymes, Models, and Intermediates. *Chem. Rev.* **2004,** *104* (2), 939-986.
21. Chavez, F. A.; Rowland, J. M.; Olmstead, M. M.; Mascharak, P. K., Syntheses, Structures, and Reactivities of Cobalt(III)−Alkylperoxo Complexes and Their Role in Stoichiometric and Catalytic Oxidation of Hydrocarbons. *J. Am. Chem. Soc.* **1998,** *120* (35), 9015-9027.
22. Chen, Y.; Shi, H.; Lee, C.-S.; Yiu, S.-M.; Man, W.-L.; Lau, T.-C., Room Temperature Aerobic Peroxidation of Organic Substrates Catalyzed by Cobalt(III) Alkylperoxo Complexes. *J. Am. Chem. Soc.* **2021,** *143* (36), 14445-14450.

23. Widger, L. R.; Jiang, Y.; McQuilken, A. C.; Yang, T.; Siegler, M. A.; Matsumura, H.; Moenne-Loccoz, P.; Kumar, D.; de Visser, S. P.; Goldberg, D. P., Thioether-ligated iron(II) and iron(III)-hydroperoxo/alkylperoxo complexes with an H-bond donor in the second coordination sphere. *Dalton Trans.* **2014,** *43*, 7522-7532.
24. Du, J.; Miao, C.; Xia, C.; Lee, Y.-M.; Nam, W.; Sun, W., Mechanistic Insights into the Enantioselective Epoxidation of Olefins by Bioinspired Manganese Complexes: Role of Carboxylic Acid and Nature of Active Oxidant. *ACS Catalysis* **2018,** *8* (5), 4528-4538.
25. Miao, C.; Wang, B.; Wang, Y.; Xia, C.; Lee, Y.-M.; Nam, W.; Sun, W., Proton-Promoted and Anion-Enhanced Epoxidation of Olefins by Hydrogen Peroxide in the Presence of Nonheme Manganese Catalysts. *J. Am. Chem. Soc.* **2016,** *138* (3), 936-943.
26. Coggins, M. K.; Martin-Diaconescu, V.; DeBeer, S.; Kovacs, J. A., Correlation Between Structural, Spectroscopic, and Reactivity Properties Within a Series of Structurally Analogous Metastable Manganese(III)–Alkylperoxo Complexes. *J. Am. Chem. Soc.* **2013,** *135* (11), 4260-4272.
27. Coggins, M. K.; Kovacs, J. A., Structural and Spectroscopic Characterization of Metastable Thiolate-Ligated Manganese(III)–Alkylperoxo Species. *J. Am. Chem. Soc.* **2011,** *133* (32), 12470-12473.
28. Downing, A. N.; Coggins, M. K.; Poon, P. C. Y.; Kovacs, J. A., Influence of Thiolate versus Alkoxide Ligands on the Stability of Crystallographically Characterized Mn(III)-Alkylperoxo Complexes. *J. Am. Chem. Soc.* **2021,** *143* (16), 6104-6113.
29. Parham, J. D.; Wijeratne, G. B.; Rice, D. B.; Jackson, T. A., Spectroscopic and Structural Characterization of Mn(III)-Alkylperoxo Complexes Supported by Pentadentate Amide-Containing Ligands. *Inorg. Chem.* **2018,** *57* (5), 2489-2502.
30. Opalade, A. A.; Parham, J. D.; Day, V. W.; Jackson, T. A., Characterization and chemical reactivity of room-temperature-stable MnIII–alkylperoxo complexes. *Chem. Sci.* **2021,** *12*, 12564-12575.
31. Neese, F., Software update: the ORCA program system, version 4.0. *Wiley Interdisciplinary Reviews: Computational Molecular Science* **2018,** *8* (1), e1327.
32. Neese, F., The ORCA program system. *Wiley Interdisciplinary Reviews: Computational Molecular Science* **2012,** *2* (1), 73-78.
33. Tao, J.; Perdew, J. P.; Staroverov, V. N.; Scuseria, G. E., Climbing the Density Functional Ladder: Nonempirical Meta-Generalized Gradient Approximation Designed for Molecules and Solids. *Phys. Rev. Lett.* **2003,** *91* (14), 146401.
34. Grimme, S.; Antony, J.; Ehrlich, S.; Krieg, H., A consistent and accurate ab initio parametrization of density functional dispersion correction (DFT-D) for the 94 elements H-Pu. *J. Chem. Phys.* **2010,** *132* (15), 154104.
35. Grimme, S.; Ehrlich, S.; Goerigk, L., Effect of the damping function in dispersion corrected density functional theory. *Journal of Computational Chemistry* **2011,** *32* (7), 1456-1465.
36. Schäfer, A.; Horn, H.; Ahlrichs, R., Fully optimized contracted Gaussian basis sets for atoms Li to Kr. *J. Chem. Phys.* **1992,** *97* (4), 2571-2577.
37. Weigend, F.; Ahlrichs, R., Balanced basis sets of split valence, triple zeta valence and quadruple zeta valence quality for H to Rn: Design and assessment of accuracy. *PCCP* **2005,** *7* (18), 3297-3305.
38. Neese, F.; Wennmohs, F.; Hansen, A., Efficient and accurate local approximations to coupled-electron pair approaches: An attempt to revive the pair natural orbital method. *The Journal of Chemical Physics* **2009,** *130* (11), 114108.

39. Our DFT calculations identified several quintet transition states, suggesting a relatively flat surface near the transition state. The different transition states had slight variations in O-O distance (~2.3 – 2.44 Å), with shorter O-O distances giving slightly higher imaginary frequencies (-130 cm-1). Importantly, however, the total energies of these transition states varied by only ~1 kcal mol-1. Thus, the chosen transition state discussed in the main text and figures is representative of this set.
40. Halbach, R. L.; Gygi, D.; Bloch, E. D.; Anderson, B. L.; Nocera, D. G., Structurally characterized terminal manganese(iv) oxo tris(alkoxide) complex. *Chem. Sci.* **2018,** *9* (19), 4524-4528.
41. Leto, D. F.; Jackson, T. A., Mn K-Edge X-ray Absorption Studies of Oxo- and Hydroxo-manganese(IV) Complexes: Experimental and Theoretical Insights into Pre-Edge Properties. *Inorg. Chem.* **2014,** *53* (12), 6179-6194.
42. Chen, J.; Lee, Y.-M.; Davis, K. M.; Wu, X.; Seo, M. S.; Cho, K.-B.; Yoon, H.; Park, Y. J.; Fukuzumi, S.; Pushkar, Y. N.; Nam, W., A Mononuclear Non-Heme Manganese(IV)–Oxo Complex Binding Redox-Inactive Metal Ions. *J. Am. Chem. Soc.* **2013,** *135*, 6388-6391.
43. Wu, X.; Seo, M. S.; Davis, K. M.; Lee, Y.-M.; Chen, J.; Cho, K.-B.; Pushkar, Y. N.; Nam, W., A Highly Reactive Mononuclear Non-Heme Manganese(IV)–Oxo Complex That Can Activate the Strong C–H Bonds of Alkanes. *J. Am. Chem. Soc.* **2011,** *133* (50), 20088-20091.
44. Leto, D. F.; Ingram, R.; Day, V. W.; Jackson, T. A., Spectroscopic properties and reactivity of a mononuclear oxomanganese(iv) complex. *Chem. Commun.* **2013,** *49* (47), 5378-5380.
45. Chen, J.; Yoon, H.; Lee, Y.-M.; Seo, M. S.; Sarangi, R.; Fukuzumi, S.; Nam, W., Tuning the reactivity of mononuclear nonheme manganese(iv)-oxo complexes by triflic acid. *Chem. Sci.* **2015,** *6* (6), 3624-3632.
46. Massie, A. A.; Denler, M. C.; Singh, R.; Sinha, A.; Nordlander, E.; Jackson, T. A., Structural Characterization of a Series of N5-Ligated MnIV-Oxo Species. *Chem. Eur. J.* **2020,** *26* (4), 900-912.
47. Rice, D. B.; Massie, A. A.; Jackson, T. A., Experimental and Multireference ab Initio Investigations of Hydrogen-Atom-Transfer Reactivity of a Mononuclear MnIV-oxo Complex. *Inorg. Chem.* **2019,** *58* (20), 13902-13916.
48. Cho, K.-B.; Shaik, S.; Nam, W., Theoretical Investigations into C–H Bond Activation Reaction by Nonheme MnIVO Complexes: Multistate Reactivity with No Oxygen Rebound. *The Journal of Physical Chemistry Letters* **2012,** *3* (19), 2851-2856.
49. Chen, J.; Cho, K.-B.; Lee, Y.-M.; Kwon, Y. H.; Nam, W., Mononuclear nonheme iron(iv)-oxo and manganese(iv)-oxo complexes in oxidation reactions: experimental results prove theoretical prediction. *Chem. Commun.* **2015,** *51* (66), 13094-13097.
50. Massie, A. A.; Denler, M. C.; Cardoso, L. T.; Walker, A. N.; Hossain, M. K.; Day, V. W.; Nordlander, E.; Jackson, T. A., Equatorial Ligand Perturbations Influence the Reactivity of Manganese(IV)-Oxo Complexes. *Angew. Chem. Int. Ed.* **2017,** *56* (15), 4178-4182.
51. Mayfield, J. R.; Grotemeyer, E. N.; Jackson, T. A., Concerted proton–electron transfer reactions of manganese–hydroxo and manganese–oxo complexes. *Chem. Commun.* **2020,** *56* (65), 9238-9255.
52. We also considered formation of a product where the O^{t}Bu fragment is directly coordinated to the Mn center to give a $[Mn(O)(O^tBu)(N4S)]^+$ species. During the DFT optimization of this complex, one of the 6-Me-pyridyl groups of the N4S ligand decoordinated from the Mn center to accommodate coordination of the bulky O^{t}Bu fragment. The electronic energy of this complex is 10.6 kcal mol^{-1} relative to the quintet reactant, making this species a fairly low

energy product. However, because this species has an entropy similar to that of the reactant, the free energy change of this product is slightly less favorable than the O-O cleavage product discussed in the main text.
53. Coggins, M. K.; Brines, L. M.; Kovacs, J. A., Synthesis and Structural Characterization of a Series of $Mn^{III}OR$ Complexes, Including a Water-Soluble MnIIIOH That Promotes Aerobic Hydrogen-Atom Transfer. *Inorg. Chem.* **2013,** *52* (21), 12383-12393.